

Evolution of Giant Planets in Eccentric Disks[†]

GENNARO D'ANGELO¹

School of Physics, University of Exeter, Stocker Road, Exeter EX4 4QL, United Kingdom
NASA-ARC, Space Science and Astrobiology Division, MS 245-3, Moffett Field, CA 94035, USA
gdangelo@arc.nasa.gov

AND

STEPHEN H. LUBOW

Space Telescope Science Institute, 3700 San Martin Drive, Baltimore, MD 21218, USA
lubow@stsci.edu

AND

MATTHEW R. BATE

School of Physics, University of Exeter, Stocker Road, Exeter EX4 4QL, United Kingdom
mbate@astro.ex.ac.uk

ABSTRACT

We investigate the interaction between a giant planet and a viscous circumstellar disk by means of high-resolution, two-dimensional hydrodynamical simulations. We consider planet masses that range from 1 to 3 Jupiter masses (M_J) and initial orbital eccentricities that range from 0 to 0.4. We find that a planet can cause eccentricity growth in a disk region adjacent to the planet's orbit, even if the planet's orbit is circular. Disk-planet interactions lead to growth in a planet's orbital eccentricity. The orbital eccentricities of a $2 M_J$ and a $3 M_J$ planet increase from 0 to 0.11 within about 3000 orbits. Over a similar time period, the orbital eccentricity of a $1 M_J$ planet grows from 0 to 0.02. For a case of a $1 M_J$ planet with an initial eccentricity of 0.01, the orbital eccentricity grows to 0.09 over 4000 orbits. Radial migration is directed inwards, but slows considerably as a planet's orbit becomes eccentric. If a planet's orbital eccentricity becomes sufficiently large, $e \gtrsim 0.2$, migration can reverse and so be directed outwards. The accretion rate towards a planet depends on both the disk and the planet orbital eccentricity and is pulsed over the orbital period. Planet mass growth rates increase with planet orbital eccentricity. For $e \sim 0.2$ the mass growth rate of a planet increases by $\sim 30\%$ above the value for $e = 0$. For $e \gtrsim 0.1$, most of the accretion within the planet's Roche lobe occurs when the planet is near the apocenter. Similar accretion modulation occurs for flow at the inner disk boundary which represents accretion toward the star.

Subject headings: accretion, accretion disks — hydrodynamics — methods: numerical — planetary systems: formation

1. Introduction

A striking property of the extrasolar planets known to date is the range of their orbital eccentricities, which is far wider than that of planets in the solar system.² Eccentricities are typically $\sim 0.2\text{--}0.3$, but very low and high values are also found (e.g., Marcy et al. 2005). A variety of explanations

have been proposed to explain the eccentricities. The high eccentricity cases may owe their explanation to the presence of a distant binary companion (Wu & Murray 2003; Takeda & Rasio 2005). In fact, the large eccentricity ($e = 0.93$) of HD 80606b could be the result of a three-body interaction process, known as “Kozai cycle” (Wu & Murray 2003). Moreover, numerical experiments show that the observed distribution of orbital eccentricities for $e \gtrsim 0.6$ can be reproduced by assuming the action of a Kozai-type perturbation (Takeda & Rasio 2005).

For more typical eccentricities, other processes are likely to be at work. Planet-planet interactions involving scattering on dynamical timescales is a possibility (Rasio & Ford

[†]To appear in THE ASTROPHYSICAL JOURNAL (v652 n2 December 1, 2006 issue).

¹NASA Postdoctoral Fellow.

²See the California & Carnegie Planet Search at <http://exoplanets.org> and the Extrasolar Planets Encyclopaedia at <http://exoplanet.eu>.

1996). However, numerical experiments indicate that interactions between equal mass planets would produce more isolated planets on low-eccentricity orbits than those observed (Ford et al. 2001). Secular interactions between planets is another possible means of eccentricity excitation (Juric & Tremaine 2005). This mechanism assumes that the planets have appropriate initial separations for evolution to occur on secular timescales ($\sim 10^{10}$ years).

Disk-planet interactions can also give rise to planetary eccentricities (Goldreich & Tremaine 1980; Artyomowicz 1992; Goldreich & Sari 2003). The evolution of orbital eccentricity depends on a delicate balance between Lindblad and corotation resonances. If the planet is massive enough to clear a gap, Lindblad resonances promote eccentricity growth, while corotation resonances damp eccentricity. If the corotation resonances operate at maximal efficiency, they dominate over Lindblad resonances by a slight margin, and the result is eccentricity damping (Goldreich & Tremaine 1980). Two mechanisms have been proposed to weaken the effects of corotation resonances and thereby provide eccentricity growth. The first mechanism relies on a large enough gap about a planet's orbit to exclude the corotation resonances from the disk, while leaving a remaining Lindblad resonance, the 1:3 outer resonance. This mechanism requires a massive enough companion and/or low enough viscosity to open a wide enough gap. Such a mechanism has been demonstrated for binary stars (Artyomowicz et al. 1991). The second mechanism relies on the delicate nature of corotational resonances in their ability to weaken (saturate) when the disk viscosity is sufficiently small and the planet eccentricity sufficiently large (Ogilvie & Lubow 2003; Goldreich & Sari 2003). A small finite initial eccentricity, typically $e \sim 0.01$, is required for the eccentricity to grow by this mechanism. Moreover, a companion object on a circular orbit can drive eccentricity in a circumstellar disk. This process is believed to occur in disks involving 10–20 Jupiter-mass (M_J) companions (Papaloizou et al. 2001) and binary stars (Lubow 1991a,b). The disk transfers eccentricity to the planet's orbit by exchanging energy and angular momentum. The disk-planet system undergoes a coupled eccentricity evolution.

One goal of this paper is to determine whether the eccentricity growth by disk-planet interactions occurs. Simulations by Papaloizou et al. (2001) suggested that orbital eccentricity is excited when the mass of the embedded body is larger than about 10–20 Jupiter-masses, while lower mass companions experienced eccentricity damping. By applying higher resolution and simulating over longer timescales, we aim to see whether eccentricity growth can occur for lower mass, planetary mass, companions. In addition, we are interested in the effects of eccentricity on planet migration.

Accretion of gas onto a planet is likely affected by the planet's orbit eccentricity. Circumbinary disks surrounding eccentric orbit binaries undergo pulsed accretion on orbital timescales (Artyomowicz & Lubow 1996). A similar process could occur with eccentric orbit planets. The mean accretion rate could also be modified by the orbital eccentricity. Another goal of this paper is to investigate this accretion process.

We apply high-resolution hydrodynamical simulations to

investigate disk-planet interactions over several thousand orbital periods. In Section 2 we describe the physical model. The numerical aspects of the calculations are detailed in Section 3. Results on the growth of the disk eccentricity for a fixed planet orbit are presented in Section 4. Similar results on the growth of disk eccentricity were recently reported by Kley & Dirksen (2006). We describe results on the planet's orbital evolution in Section 5. Results on the pulsed accretion are described in Section 6. Finally, our conclusions are given in Section 7

2. Model Description

2.1. Evolution Equations

We assume that the disk matter and planet are in coplanar orbits. In order to describe the dynamical interactions between a circumstellar disk and a giant planet, we approximate the disk as being two-dimensional, by ignoring dynamical effects in the direction perpendicular to the orbit plane (vertical direction). This approximation is justified by the fact that the disk thickness is smaller than the vertical extent of the planetary Roche lobes for the cases we consider. Comparisons between two- and three-dimensional models of Jupiter-mass planets embedded in a disk indicate that the two-dimensional geometry provides a sufficiently reliable description of the system (Kley et al. 2001; D'Angelo et al. 2003; Bate et al. 2003; D'Angelo et al. 2005).

We employ a cylindrical coordinate frame $\{O; r, \phi, z\}$ in which the disk lies in the plane $z = 0$ and the origin, O , is located on the primary. The reference frame rotates about the disk axis (i.e., the z -axis) with an angular velocity Ω and an angular acceleration $\dot{\Omega}$. The set of continuity and momentum equations, describing the evolution of the disk, is written in a conservative form (see, e.g, D'Angelo et al. 2002) and is solved for the surface density, Σ , and the velocity field of the fluid, \mathbf{u} . The turbulent viscosity forces in the disk are assumed to arise from a standard viscous stress tensor for a Newtonian fluid with a constant kinematic viscosity, ν , and a zero bulk viscosity (see Mihalas & Weibel Mihalas 1999, for details).

A locally isothermal equation of state is adopted by requiring that the vertically integrated pressure is equal to $p = c_s^2 \Sigma$ and that the sound speed, c_s , is equal to the disk aspect ratio, H/r , times the Keplerian velocity. In this study, we use a constant aspect ratio throughout the disk.

The gravitational potential of the disk, Φ , is given by

$$\Phi = -\frac{G M_*}{|r|} - \frac{G M_p}{\sqrt{|r - r_p|^2 + \varepsilon^2}} + \frac{G M_p}{|r_p|^3} \mathbf{r} \cdot \mathbf{r}_p, \quad (1)$$

where M_* is the mass of the central star whereas M_p and \mathbf{r}_p are the mass and the vector position of the planet, respectively. The length ε represents a softening length that is needed to avoid singularities in the gravitational potential of the planet. The third term on the right-hand side of equation (1) accounts for the acceleration of the origin of the (non-inertial) coordinate frame caused by the planet. We ignore disk self-gravity. For the disks we consider, the Toomre- Q parameter never drops below 4 during the simulations.

The orbit of the planet evolves under the gravitational forces exerted by the central star and the disk material. Non-inertial forces arising from the rotation of the reference frame also need to be taken into account. Therefore, the equation of motion of the planet reads

$$\ddot{\mathbf{r}}_p = -\frac{G(M_* + M_p)}{|r_p|^3} \mathbf{r}_p - \boldsymbol{\Omega} \times (\boldsymbol{\Omega} \times \mathbf{r}_p) - 2\boldsymbol{\Omega} \times \dot{\mathbf{r}}_p - \dot{\boldsymbol{\Omega}} \times \mathbf{r}_p + \mathbf{A}_p - \mathbf{A}_*, \quad (2)$$

where the angular velocity and acceleration vectors of the rotating frame are defined as $\boldsymbol{\Omega} = \Omega \hat{z}$ and $\dot{\boldsymbol{\Omega}} = \dot{\Omega} \hat{z}$, respectively. The second, third, and fourth terms on the right-hand side of the equation are the centrifugal, Coriolis, and angular accelerations, respectively.

The angular velocity of the reference frame relative to a fixed frame, $\Omega = \Omega(t)$, is chosen so as to compensate for the azimuthal motion of the planet. Details of how this is achieved can be found in D'Angelo et al. (2005). Since the azimuthal position of the planet is constant, a circular orbit reduces to a fixed point in the rotating frame. For a planet orbit with $e > 0$, the planet radially oscillates between the pericenter distance, $a(1-e)$, and the apocenter distance, $a(1+e)$. In this frame, the trajectory is a straight line of length $2ae$ with center at $r = a$. This scheme has the advantage that the planet does not drift across the grid in the azimuthal direction. It always maintains a symmetric azimuthal position with respect to the zone centers (where eqs. [1], [3], and [4] are evaluated) while it moves radially. This method helps reduce artificially unbalanced forces that act on the protoplanet (see discussion in Nelson & Benz 2003a,b).

The last two terms in equation (2), which represent the forces per unit mass exerted by the disk material on the planet and the star, are

$$\mathbf{A}_p = G \int_{M_D} \frac{(\mathbf{r} - \mathbf{r}_p) dM_D(\mathbf{r})}{(|\mathbf{r} - \mathbf{r}_p|^2 + \varepsilon^2)^{3/2}} \quad (3)$$

and

$$\mathbf{A}_* = G \int_{M_D} \frac{\mathbf{r} dM_D(\mathbf{r})}{r^3}. \quad (4)$$

These two vectors are included in equation (2) only when the disk back-reaction is accounted for and the protoplanet is allowed to adjust its trajectory in response to the disk torques. When these terms are applied, the integration in equations (3) and (4) is performed over the disk mass comprised in the simulated domain, M_D .

2.2. Physical Parameters

In these calculations, the stellar mass, M_* , is the unit of mass and the initial semi-major axis of the planet's orbit, a_0 , represents the unit of length. The unit of time, t_0 , is defined such that $1/t_0 = \sqrt{G(M_* + M_p)/a_0^3}$. When we refer to the “orbital period” or “orbit” as length of time, we actually mean the initial orbital period $t_0/(2\pi)$. To provide estimates of various quantities in physical units, we adopt $M_* = 1 M_\odot$ and $a_0 = 5.2$ AU, thus one orbit is ≈ 11.9 years.

In order to treat the strong perturbations induced by giant protoplanets and limit the influence of the imposed radial boundaries, we considered an extended disk whose radial

borders are at $r_{\min} = 0.3 a_0$ and $r_{\max} = 6.5 a_0$. The disk extends over the entire 2π radians in azimuth around the star. In physical units, the disk models cover a region from 1.56 to 33.8 AU. The mass of the disk, in the absence of the planet, is $M_D = 1.58 \times 10^{-2} M_*$ within the radial limits of the simulated region. We used a constant disk aspect ratio, $H/r = 0.05$. The unperturbed initial surface density is axisymmetric and scales as $r^{-1/2}$, which produces an unperturbed density, at $r = a_0$, equal to 75.8 g cm^{-2} . However, given the large planetary masses considered in this investigation, we also included an initial gap along the orbit of the planet that accounts for an approximate balance between viscous and tidal torques (e.g., Lin & Papaloizou 1986). The initial gap profile is based on equation (5) of Lubow & D'Angelo (2006). The initial gap width is modified by a factor of $1 + a_0 e_0$, in order to account for the planet's initial orbital eccentricity, e_0 .

The initial velocity field in the disk is a Keplerian one that is centered on the star and corrected for the rotation of the frame of reference. In order to account for the effects due to turbulence in the disk, a constant kinematic viscosity, ν , was used. In terms of the Shakura & Sunyaev parameter (Shakura & Sunyaev 1973), we have $\alpha = \alpha_0 (a_0/r)^{1/2}$, where $\alpha_0 = 4 \times 10^{-3}$ (in physical units, $\nu \simeq 10^{15} \text{ cm}^2 \text{ s}^{-1}$). Although spatial variations and time fluctuations consistent with the MHD turbulence are not included, this relation yields a magnitude of α that is in the range found in MHD simulations (Papaloizou & Nelson 2003; Winters et al. 2003; Nelson & Papaloizou 2004). The influence of viscosity was explored by performing a few calculations with other α_0 values (1.2×10^{-3} and 1.2×10^{-2}).

Three planetary masses were considered: $1 M_J$, $2 M_J$, and $3 M_J$ (i.e., the mass ratio $q = M_p/M_*$ ranges from 1×10^{-3} to 3×10^{-3}). The planets were set on initially circular or eccentric orbits about one solar mass stars. We examined configurations with initial eccentricities, e_0 , up to 0.4. A complete list is given in Table 1.

At time $t = 0$ the planet starts from the pericenter position, while its azimuth, ϕ_p , remains constant (in the rotating frame) and equal to π throughout the calculation. In order to allow the disk to adjust to the presence of the planet, we impose two stages to the evolution. During the first phase, the planet's orbit is static and terms (3) and (4) are not included in equation (2). During the second phase, the protoplanet is “released” from the fixed orbit and is allowed to react to the disk torques via the full form of equation (2). In the models presented here the first phase lasts until the release time, $t = t_{\text{rls}}$, which ranges from 1000 to 1200 orbits. The second phase lasts from several hundred to several thousand orbits.

The value adopted for smoothing radius ε (in eqs. [1] and [3]) resulted from numerical experiments in each orbital eccentricity configuration. The chosen value of ε was the smallest that prevented the integration time-step of the hydrodynamics equations from getting shorter than $\sim 10^{-6}$ orbits. In models involving $1 M_J$ and $2 M_J$ planets, we set $\varepsilon = 0.1 R_H$, where $R_H = r_p (q/3)^{1/3}$ (Bailey 1972) is planet's Hill radius (or sometimes called Roche radius). In models involving $3 M_J$ planets, we applied softening lengths between $0.12 R_H$ and $0.2 R_H$. The latter value was used at the highest initial orbital

TABLE 1
INITIAL ORBITAL ECCENTRICITIES.

M_p (M_J)	e_0					
	0	0.01	0.1	0.2	0.3	0.4
1	•	•	•	•	•	•
2	•					
3	•		•	•	•	•

eccentricities, $e_0 = 0.3$ and 0.4 . We found that torques within the Roche lobe do not dominate the planet orbital evolution. Moreover, the smoothing radius does not significantly affect planet accretion. Thus, ε does not likely play an important role in these calculations.

For simulations that account for the disk torques on the planet, an additional approximation is made, which is described at the beginning of Section 5.

3. Numerical Method

The equations of motion of the disk are solved numerically by means of a finite-difference scheme that uses a directional operator splitting procedure. The method is second-order accurate in space and semi-second-order in time (Ziegler & Yorke 1997). Hydrodynamic variables are advected by means of a transport scheme that uses a piecewise linear reconstruction of the variables with a monotonised slope limiter (van Leer 1977). High numerical resolution in an extended region around the planet is achieved by using a nested-grid technique (see D'Angelo et al. 2002, 2003, for details) with fully nested subgrid patches, whereby each subgrid level increases the resolution by a factor 2 in each direction. Tests on the behavior of the nested-grid technique applied in a reference frame rotating at a variable rate $\Omega = \Omega(t)$ are reported in the Appendix of D'Angelo et al. (2005). The equation of motion of the planet (eq. [2]) is solved by using a high-accuracy algorithm described in D'Angelo et al. (2005).

3.1. Grid Resolution

The excitation or damping of a protoplanet's orbital eccentricity depends on a delicate balance between Lindblad and corotation resonances (Ogilvie & Lubow 2003; Goldreich & Sari 2003, and references therein). To study this balance, it is necessary to resolve the width of all the resonances involved in the process. The locations of first order eccentric Lindblad resonances reside in a region that ranges radially from approximately $0.6a$ to $1.6a$. Furthermore, calculations on the saturation of isolated noncoorbital corotation resonances, performed by Masset & Ogilvie (2004), suggest that a minimum resolution requirement to avoid spurious damping of eccentricity is that

$$\Delta r/a \lesssim 4.1 \sqrt{C_k^\pm k e q}, \quad (5)$$

where k is the azimuthal wavenumber and C_k^\pm are coefficients of order unity given in Ogilvie & Lubow (2003). Although nested grids provide a linear resolution ≤ 0.01 in a region $\sim 2.5a \times 0.8\pi$, the effects of these corotational resonances are not localized in azimuth, so the nested grids do not substantially improve their overall resolution. Calculations that follow the orbital evolution of the planet were executed with grid systems GS1 and GS2 (see Table 2 for a description of all grid systems employed in this study). According to equation (5), the global radial resolution we apply $\Delta r/a = 0.02$ could produce spurious damping in the outer disk for orbital eccentricities $e \lesssim 3 \times 10^{-5}/(k q)$, with $k > 1$. In the $1 M_J$ case, simulations with $0.01 < e < 0.015$ could undergo spurious eccentricity damping for the most distant outer resonance $k = 2$ only. For $e > 0.015$, there is no spurious damping. In the $3 M_J$ case, simulations with $0.003 < e < 0.005$ could undergo spurious damping for $k = 2$ only. For $e > 0.005$, there is no spurious damping.

3.2. Mass Accretion Procedure

Accretion onto the protoplanet was simulated by removing material within a distance of $r_{\text{acc}} = 0.3 R_H$. Mass is removed by means of a two-step procedure according to which the removal timescale, τ_{acc} , is 0.03 orbital periods for $|\mathbf{r} - \mathbf{r}_p| < r_{\text{acc}}/2$ and 0.09 orbital periods in the outer part of the accretion region, $r_{\text{acc}}/2 < |\mathbf{r} - \mathbf{r}_p| < r_{\text{acc}}$. Notice that τ_{acc} is about equal to the Keplerian period around the protoplanet (i.e., in the circumplanetary disk) at $|\mathbf{r} - \mathbf{r}_p| = r_{\text{acc}}/2$. Tests were carried out to evaluate the sensitivity of the procedure to both parameters r_{acc} and τ_{acc} . These tests indicate that, if r_{acc} is reduced by a factor of 1.5, the average mass accreted during an orbit varies by less than 10%. Increasing the removal timescale by a factor of 5/3 only affects the accretion rate by 5% (see also Tanigawa & Watanabe 2002). We also checked whether the accretion parameters influence the orbital evolution of the planet. Using the same tests, we found no significant differences over a few hundred periods of evolution.

We do not add the removed mass to the planet mass over the course of the simulations. Doing so would increase the planet mass by $\sim 1 M_J$ for the simulations reported here.

TABLE 2
GRID SYSTEMS USED IN THE SIMULATIONS.

Grid level	GS1 $N_r \times N_\phi$	GS2 $N_r \times N_\phi$	GS3 $N_r \times N_\phi$	GS4 $N_r \times N_\phi$
1	313×317	313×317	623×629	623×629
2	264×264	264×264	524×524	
3		404×404		

NOTE.—The grid system GS1 achieves the highest resolution $(\Delta r/a_0, \Delta\phi) = (0.01, 0.01)$ in the region $(r, \phi) \in [0.4, 3.0] a_0 \times 0.83\pi$, which is azimuthally centered on the planet. The grid system GS3 resolve the same region with a resolution $(\Delta r/a_0, \Delta\phi) = (0.005, 0.005)$. The latter resolution is obtained with the grid system GS2 in the region $(r, \phi) \in [0.5, 2.5] a_0 \times 0.65\pi$ (also centered on the planet in azimuth).

3.3. Boundary Conditions

Boundary conditions at the radial inner boundary, $r = r_{\min}$, allow outflow of material, i.e., the accretion flow toward the central star. The inner boundary conditions exclude inflow away from the star into the computational domain. Two types of boundary conditions were used at the outer boundary ($r = r_{\max}$): reflective and non-reflective. With the first kind, neither inflow nor outflow of material is permitted at the outer border, which behaves as a rigid wall. Although r_{\max} is much larger than the apocenter radii of the planets in the simulations, wave reflection was observed at the outer border in this case, especially when the planet orbit was eccentric.

In order to lessen the amount of wave reflection at the outer disk edge, we also applied non-reflective boundary conditions, following the approach of [Godon \(1996, 1997\)](#). In these circumstances, boundary conditions are not directly imposed on the primitive variables (i.e., Σ and \mathbf{u}), but rather on the characteristic variables (i.e., the Riemann invariants of one-dimensional flows). The basic idea is to let outflowing (inflowing) characteristics propagate through the grid boundary. The correct propagation of the flow characteristics across the border depends on how accurately the adopted solution exterior to the grid approximates the exact solution.

At both disk radial boundaries, the flow is assumed to be Keplerian around the central star. This choice could lead to some small-amplitude wave excitation at $r = r_{\max}$, since the fluid tends to orbit about the center-of-mass of the system, rather than around the central star (see also [Nelson et al. 2000](#)). The effects of such waves were checked to be unimportant as they tend to dissipate within a short distance from the outer disk boundary.

4. Disk Eccentricity

4.1. Global Density Distribution

The global surface density in the disk is plotted in Figure 1 for different planet's masses and orbital eccentricities. Left panels refer to configurations with $M_p = 1 M_J$, and right panels refer to configurations with $M_p = 3 M_J$. The orbital eccentricity increases from top ($e = 0$) to bottom ($e = 0.3$). In all of the panels, the planet is at pericenter ($r_p/a = 1 - e$). For sufficiently long evolutionary times, the inner disk (disk interior to the planet) is largely depleted because of the tidal gap produced by the planet and because the grid does not have sufficient dynamic range to cover regions close to the star where an inner disk would reside. The outer disk is tidally truncated at a radial distance that depends on both M_p and e . Figure 1 shows that the size of the truncation radius increases with planet mass and eccentricity, analogous to the case for circumbinary disks ([Artymowicz & Lubow 1994](#)). In addition, a wave or wake propagates in the outer disk. The disk truncation also be seen in Figure 2, which shows the azimuthally averaged surface density for various cases. The outer gap edge becomes less steep as the orbital eccentricity increases and does not change significantly over an orbital period, as illustrated in Figure 3.

After a few hundred orbits, the disk region near the planet becomes eccentric, even if the planet is on a circular orbit. This effect can be seen in Figure 4, which illustrates the motion (relative to the star) of the center-of-mass of the disk interior to $r = 3 a_0$ for different planetary masses and orbital eccentricities.

4.2. Mode Analysis

We performed a mode decomposition of the surface density distribution of the disk adopting an approach along the lines

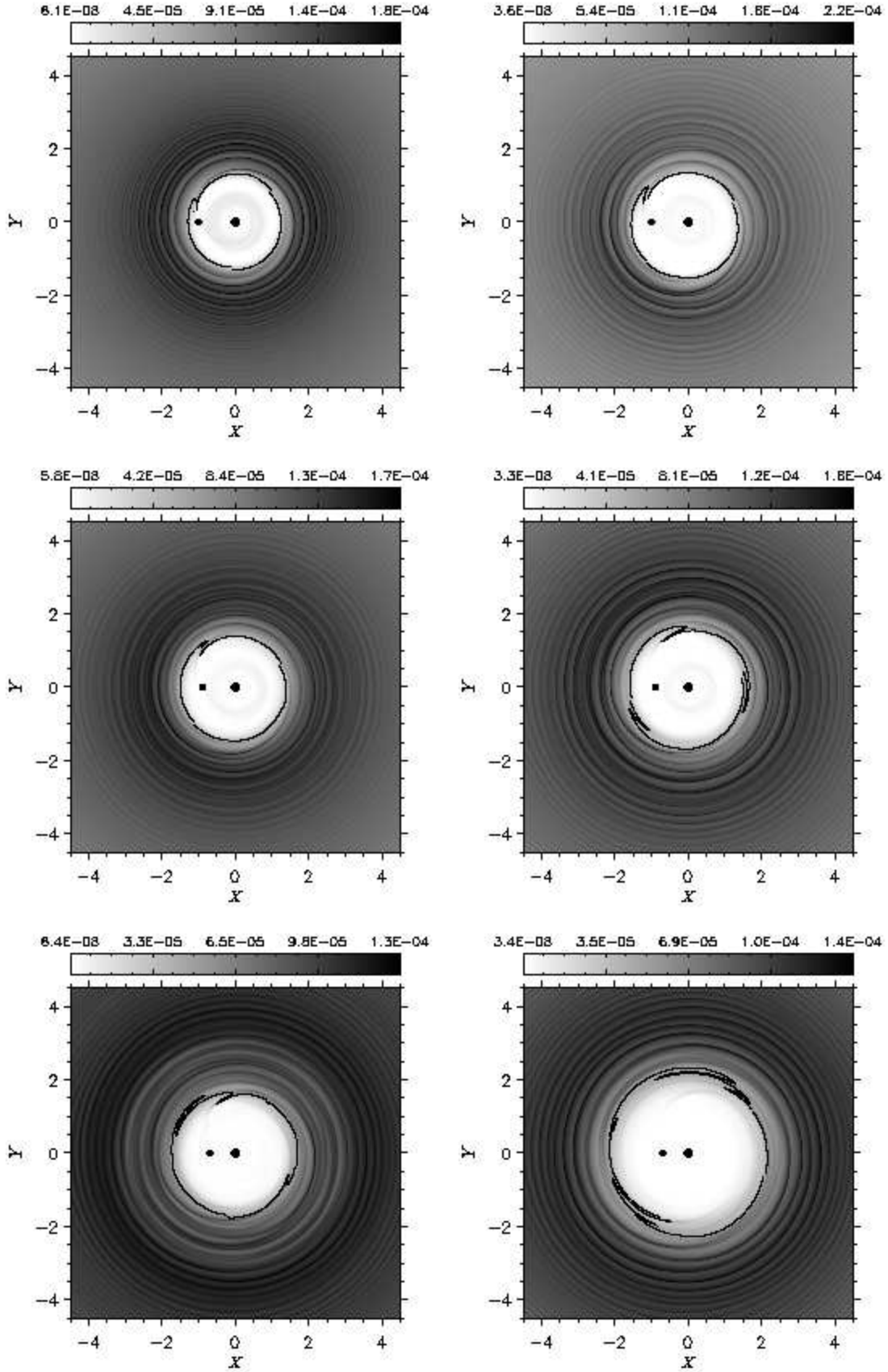


Fig. 1.— Surface density in a disk containing a $1 M_J$ (left) and a $3 M_J$ (right) planet at $t = 1000$ orbits. The axes are in units of the planet's orbital semi-major axis, a_0 . The grey scale bars are expressed in units of $3.29 \times 10^5 \text{ g cm}^{-2}$. From top to bottom, panels refer to the configurations with orbital eccentricities $e = 0, 0.1, \text{ and } 0.3$. In each panel the planet (smaller circle) is at pericenter and located at $(X, Y) = (e - 1, 0)$.

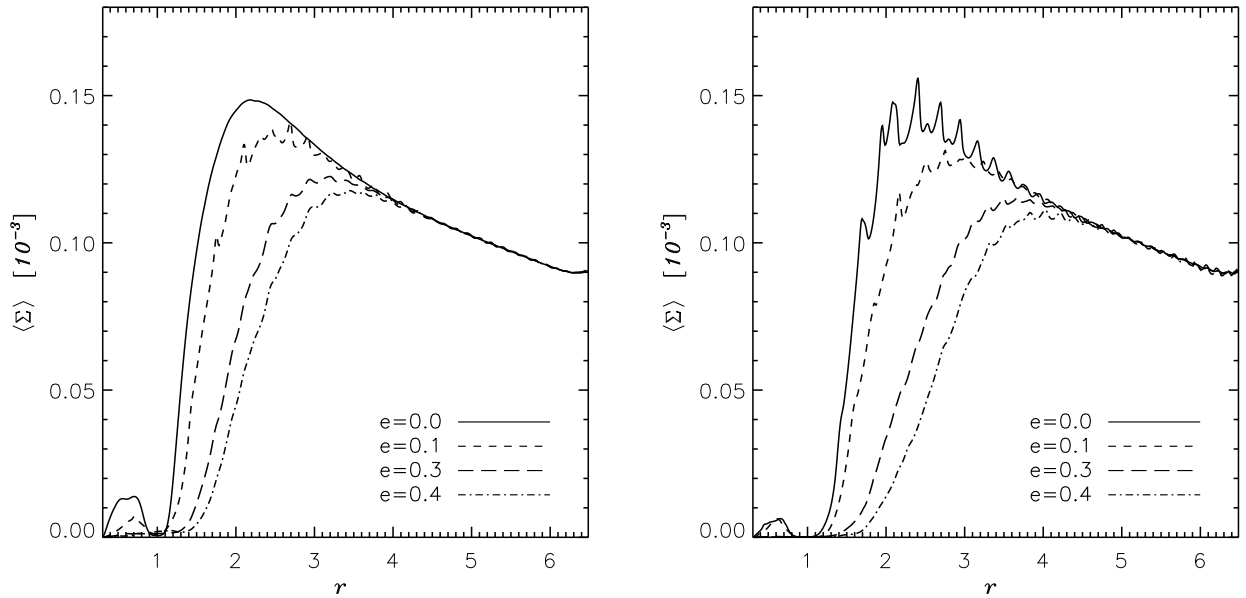


Fig. 2.— Azimuthally averaged surface density in a disk containing a $1 M_J$ (left) and $3 M_J$ (right) planet for various values of orbital eccentricity: $e = 0$ (solid line), $e = 0.1$ (short-dashed line), $e = 0.3$ (long-dashed line), and $e = 0.4$ (dotted-dashed line). The horizontal axis is in units of the planet's orbital semi-major axis a_0 . For the vertical axis, $\langle \Sigma \rangle = 10^{-4}$ corresponds to 32.9 g cm^{-2} . The time is about 1000 orbits and the planet is at pericenter.

of Lubow (1991b). We defined a mode component at each radial location in the disk as

$$\mathcal{M}_{(k,l)}^{(f,g)} = \frac{2}{\pi T \langle \Sigma \rangle (1 + \delta_{l,0})} \int_T \int_0^{2\pi} \Sigma f(k\theta) g(l\Omega_p t) d\theta dt, \quad (6)$$

where $\Omega_p = \sqrt{G(M_* + M_p)/a_0^3}$, the angle θ is the azimuth relative to an *inertial* reference frame, and $2\pi \langle \Sigma \rangle = \int_0^{2\pi} \Sigma d\theta$. The time interval T is a ten-orbit period interval, beginning at a pericenter passage of the planet. The time integration is repeated every interval T . The functions f and g are either sine or cosine. This decomposition corresponds to a Fourier transform in both azimuth and time. The amplitude (or strength) of the mode is

$$S_{(k,l)} = \left\{ \left[\mathcal{M}_{(k,l)}^{(\cos, \cos)} \right]^2 + \left[\mathcal{M}_{(k,l)}^{(\cos, \sin)} \right]^2 + \left[\mathcal{M}_{(k,l)}^{(\sin, \cos)} \right]^2 + \left[\mathcal{M}_{(k,l)}^{(\sin, \sin)} \right]^2 \right\}^{1/2}. \quad (7)$$

In order to obtain the strength of a mode integrated over a radial interval $[r_1, r_2]$, the mode components $\mathcal{M}_{(k,l)}^{(f,g)}$ are first averaged between r_1 and r_2 and then substituted into Equation (7). A tidally disturbed non-eccentric disk has modes present that all have $k = l$. For a disk ring to be eccentric, the mode strength associated with the pair $(k, l) = (1, 0)$, known as eccentric mode, must be non-zero, i.e., $S_{(1,0)} > 0$. To follow the eccentricity evolution, we analyze $S_{(1,0)}$ as a function of the time.

4.3. Eccentricity Growth

The amplitude of the eccentric mode, as defined in equation (7), is shown in Figure 5 during the evolutionary phase in which the planet is kept on a fixed orbit. This Figure refers to the configurations with $M_p = 1 M_J$, $2 M_J$, and $3 M_J$ planets having $e = 0$. The disk region that undergoes a substantial eccentricity growth is that between $r \simeq a_0$ and $r \simeq 2 a_0$ (Fig. 5, left panel). The relatively small initial value of $S_{(1,0)}$ is likely due to a transient effect, as the initially circular disk adjusts to the presence of the planet. Farther away from the planet's orbit, the mode strength drastically decreases, and the disk is nearly circular (Fig. 5, middle and right panels). The eccentricity growth proceeds very rapidly during the first 200 orbits and oscillates afterwards with some reinforcement in the $3 M_J$ case.

The eccentricity driven in the region $a_0 < r < 2 a_0$ by the $1 M_J$ planet ($e = 0$) is rather small compared to that driven by the other two planetary masses. However, with an initial orbital eccentricity $e = 0.1$, a $1 M_J$ planet is able to sustain eccentricity growth in the disk, as indicated by the solid line in the left panel of Figure 6. In the $3 M_J$ case, an initial orbital eccentricity of up to $e = 0.3$ induces a larger amplitude eccentricity perturbation only at the beginning of the evolution. But the long-term evolution of $S_{(1,0)}$ is not greatly affected (Fig. 6).

The simulations for mode analyses were generally performed with the grid GS4. We also ran simulations and computed modes by using the grid system GS1 and found results consistent to those obtained with the higher resolution grid.

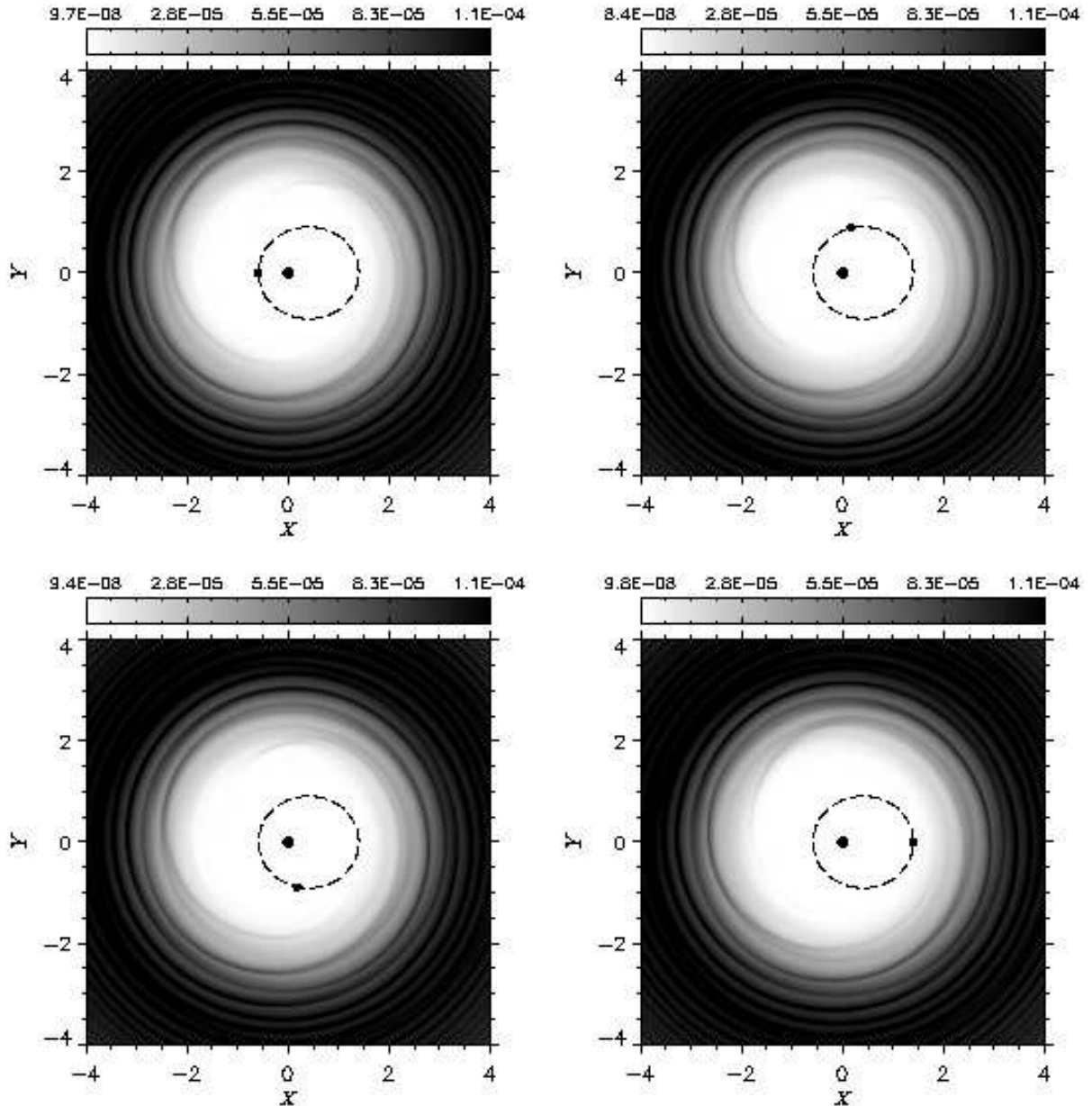


Fig. 3.— Gap region around the orbit of a $3 M_J$ planet with fixed $e = 0.4$ at various orbital phases. The axes are in units of the planet's orbital semi-major axis a_0 . The grey scale bars are expressed in units of $3.29 \times 10^5 \text{ g cm}^{-2}$. The planet's orbit in the inertial frame is represented by a dashed ellipse. The smaller solid circle indicates the position of the planet around the star (larger solid circle). The motion of the planet (and the panel sequence) is counter-clockwise.

4.3.1. Influence of Viscosity

The sensitivity of disk eccentricity growth to the disk kinematic viscosity was examined for a system containing a $3 M_J$ planet on an initially circular orbit. Two additional values of α_0 (i.e., α at $r = a_0$) were considered: $\alpha_0 = 1.2 \times 10^{-3}$ and $\alpha_0 = 1.2 \times 10^{-2}$, which are respectively a factor of 3 smaller and larger than the standard value $\alpha_0 = 4 \times 10^{-3}$. In the lowest viscosity model, the overall evolution of the amplitude of the eccentric mode closely resembles that of the model with standard viscosity (see Fig. 5, solid line), but was roughly 20% larger. In the highest viscosity model, the eccentric mode strength reached a maximum of 0.3 at $t = 200$ orbits and then decays. Around $t = 1000$ orbits, $S_{(1,0)} \approx 0.1$ and continues to decline. The effects of viscosity were also investigated with a calculation involving a $1 M_J$ planet on a circular orbit and $\alpha_0 = 1.2 \times 10^{-3}$. In this case, the mode amplitude $S_{(1,0)}$ is sustained at about 0.15 for $t > 200$ orbits, unlike the case

with standard viscosity (see Fig. 5, dashed line).

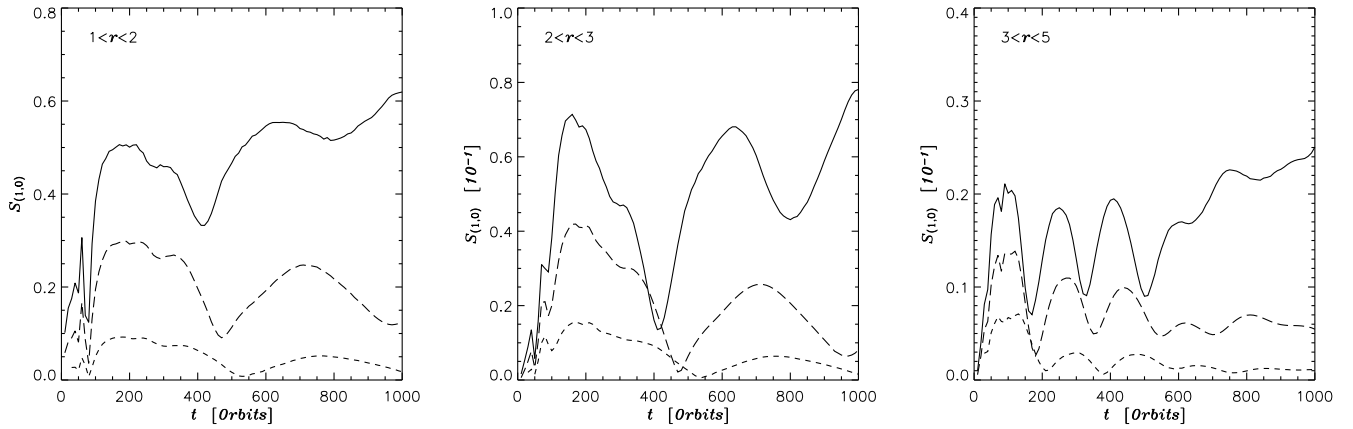


Fig. 5.— Amplitudes of the eccentric mode, associated with the pair $(k, l) = (1, 0)$ (see eq. [7]), versus time for three different disk regions, as indicated in the top-left corner of each panel, for $1 M_J$ (short-dashed), $2 M_J$ (long-dashed), and $3 M_J$ (solid) planets. In all cases, the planet resides on a fixed circular orbit. The mode strength progressively weakens as regions farther from the planet's orbit are considered.

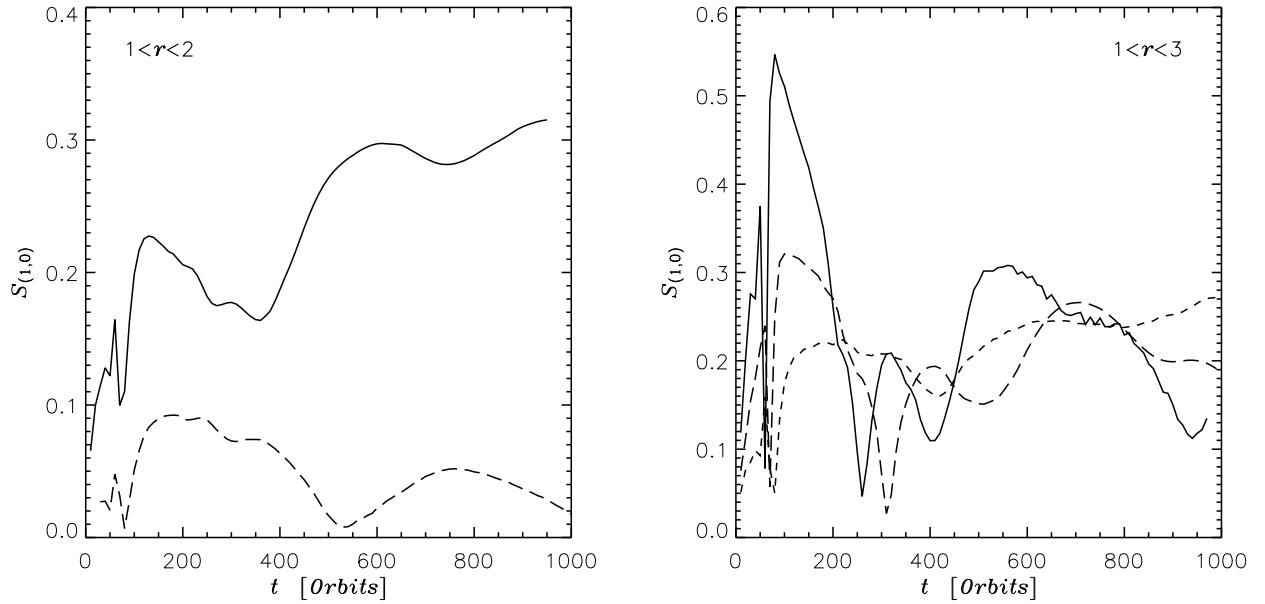


Fig. 6.— Left. Mode strength $S_{(1,0)}$ as function of time for models with $M_p = 1 M_J$ of fixed planetary orbital eccentricity $e = 0$ (dashed line) and $e = 0.1$ (solid line). Right. $S_{(1,0)}$ versus time for models with $M_p = 3 M_J$ of fixed planetary orbital eccentricity $e = 0$ (short-dashed line), $e = 0.1$ (long-dashed line), and $e = 0.3$ (solid line).

of declining eccentricity at higher viscosity that is displayed as a short-dashed line in the left panel of Figure 5. These results suggest that disks with α less than a few times 10^{-3} experience sustained eccentricity, while disks with α in excess of $\approx 10^{-2}$ do not. The weakening of disk eccentricity with viscosity was also found in simulations by [Kley & Dirksen \(2006\)](#).

4.4. Analytic Model

In the case of superhump binaries, disk precession is dominated by the gravitational effects of the companion which causes prograde precession ([Osaki 1985](#)). On the other hand, pressure provides a retrograde contribution which is somewhat weaker ([Lubow 1992; Goodchild & Ogilvie 2006](#)). In the case of a circular orbit planet, the gravitational contribution to precession is expected to be weaker than the disk's pressure contribution. The magnitude of the pressure induced precession rate is $\sim (H/r)^2 \Omega$. For the disks simulated in this paper, the precession timescale is then $\sim 10^3$ orbits. We estimated the gravitational precession due to a $3 M_J$ planet for the case plotted in Figure 5 at 1000 orbits and find that this rate is about 10 times smaller than the pressure precession rate. We then expect the precession to be pressure-dominated and retrograde, with a timescale of about 10^3 orbits. This estimate is in accord with the simulation results for a $3 M_J$ planet in a circular orbit in Figure 4.

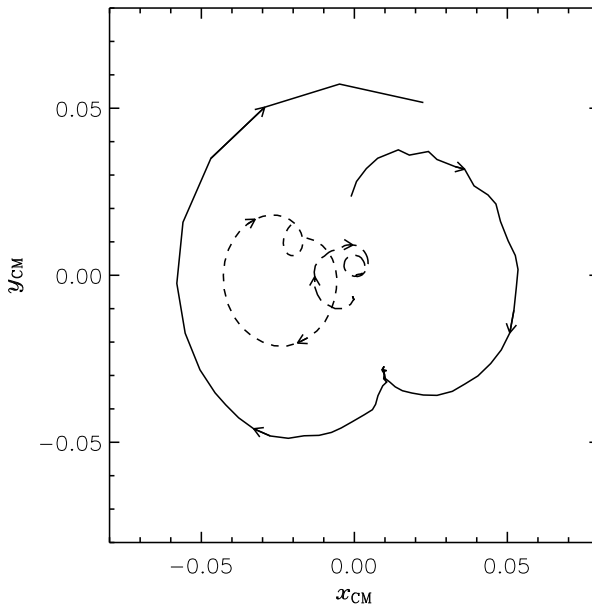


Fig. 4.— Motion of the center-of-mass of the disk region $r < 3 a_0$ relative to the star (located at the origin). The disk center-of-mass starts at the origin, but is plotted at later times $t \gtrsim 300$ orbits. The long-dashed and solid lines refer to the cases with $M_p = 1 M_J$ and $M_p = 3 M_J$, respectively, with a fixed circular orbit planet. The short-dashed line is for the model with $M_p = 3 M_J$ and fixed planet eccentricity $e = 0.1$.

The group velocity for an eccentric mode is estimated by using the dispersion relation for an $m = 1$ disturbance in a Keplerian disk perturbed by pressure. The group velocity is $v_g \sim (H/r)^2 \Omega r$, where we assume the radial wavenumber $|k_r| \sim 1/r$ and that the pattern speed is small compared to Ω . The group velocity leads to eccentricity propagation timescales of order $(r/H)^2 \sim 10^3$ orbits. This timescale is consistent with the localization of the eccentricity over course of the simulation of $\sim 10^3$ orbits to within a region of order $2 a$, as seen in Figure 6. Over longer timescales the eccentricity would spread further.

We analyze growth of eccentricity in an outer disk that is perturbed by a planet on a circular orbit. Disk eccentricity growth via the 3:1 resonance for inner disks of superhump binaries occurs on a timescale $\sim 0.1w/(rq^2)$ binary orbit periods, where w is the radial width of the eccentric region ([Lubow 1991a](#)). We now consider the case for outer disks perturbed by planets. For simplicity, we assume that the eccentric corotational resonances in the disk are saturated (i.e., of zero strength). This situation is likely to hold if the disk eccentricity is of order 0.01, by analogy with the case of an eccentric orbit planet interacting with a circular disk ([Ogilvie & Lubow 2003](#)). Following the mode coupling analysis for eccentric Lindblad resonances involving a circular orbit planet ([Lubow 1991a](#)), we find that the disk eccentricity growth rate associated with a particular eccentric outer Lindblad resonance is given by

$$\lambda_m = \frac{\pi F_m^2 \Omega_p r}{24mw}, \quad (8)$$

where

$$F_m = \frac{2ru'_m - 4rv'_m - 2u_m - m u_m + 2v_m (m - 1)}{2r\Omega_p}, \quad (9)$$

$$u_m = \frac{m(\Omega - \Omega_p)\psi'_m + 2m\Omega\psi_m/r}{\Omega^2 - m^2(\Omega - \Omega_p)^2}, \quad (10)$$

$$v_m = \frac{\Omega\psi'_m/2 + m^2(\Omega - \Omega_p)\psi_m/r}{\Omega^2 - m^2(\Omega - \Omega_p)^2}, \quad (11)$$

$$\psi_m = -q\Omega_p^2 a^2 \left[\frac{1}{\pi} \int_0^{2\pi} \frac{a \cos(\phi) d\phi}{\sqrt{a^2 + r^2 - 2ra \cos(\phi)}} - \frac{r}{a} \delta_{m,1} \right], \quad (12)$$

where w denotes the radial extent of the eccentric region and prime denotes differentiation in r . All quantities are evaluated at the location of the eccentric Lindblad resonance associated with azimuthal wavenumber m , having $\Omega = m\Omega_p/(m+2)$ and $r = r_m = [(m+2)/m]^{2/3} a$. Quantities u_m and v_m are the velocity components in a circular disk associated with potential ψ_m , and δ is the Kronecker delta function in the indirect potential term.

The combined effects of all the resonances is determined by the local disk density at each resonance. The growth rate of the mass-weighted eccentricity is then

$$\lambda = \frac{2\pi w}{M_e} \sum_{m=1}^{m_{\max}} \Sigma_m r_m \lambda_m, \quad (13)$$

where M_e is the mass of the eccentric region and the sum is taken over the active eccentric Lindblad resonances, and

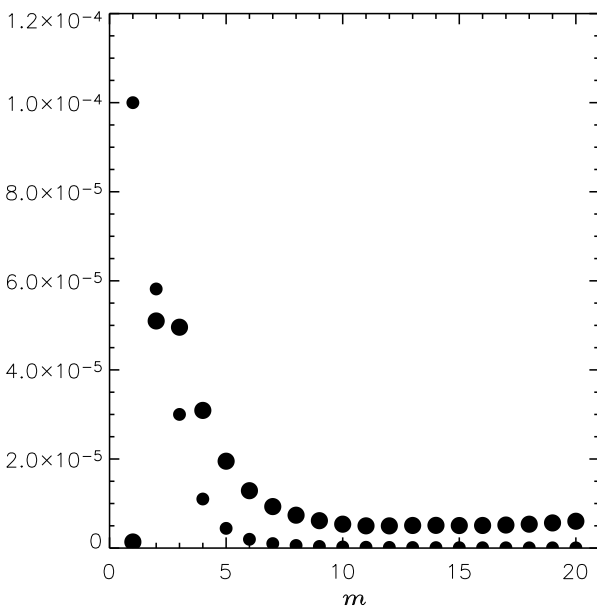


Fig. 7.— Large dots: contributions to the growth rate sum for Equation (13) in units of Ω_p as a function of azimuthal wavenumber m associated with an eccentric Lindblad resonance. Small dots: normalized azimuthally averaged surface density at each eccentric Lindblad resonance, $10^{-4} \Sigma_m / \Sigma_1$, as a function of m . The plot is for a $3 M_J$ planet with a density profile obtained from simulations at 500 orbits.

$m_{\max} \simeq r/H$ due to torque cut-off effects (Goldreich & Tremaine 1980).

The contribution of each resonance in the above sum for λ for a $3 M_J$ planet is shown in Figure 7. We consider times beyond several hundred orbits, when the width of the eccentric region $w \sim 2a$. Figure 7 shows that there is a weak contribution from the outermost resonance, the 1:3 resonance, corresponding to $m = 1$. Even though the density at this resonance is the largest, a nearly complete cancellation occurs in λ_1 , due to effects of the indirect term in potential ψ_1 . If only the $m = 1$ resonance were involved, then the eccentricity growth timescale would be very long, $\sim 10^5$ orbits. The growth rate contributions from regions closer to the planet are weakened by the lower density, but strengthened by the larger values of λ_m . At a time of 500 orbits, the density near the planet is small enough that the outermost resonances ($2 < m \lesssim 5$) provide most of the growth rate. At a time of 500 orbits, the eccentricity growth timescale $1/\lambda$ is about 600 orbits, which is in very rough agreement with the average growth rate implied by Figure 5 for the innermost region, although there are considerable fluctuations in the simulations.³ At earlier times,

³To compare the growth rate defined by λ with simulations, it is better to adopt a similar mass-weighted eccentricity. This requires a slightly different definition of $S_{(1,0)}$ than given by Equation (6). When we apply that definition, we obtain eccentric disk evolution in the $3 M_J$ case that is similar to the $3 M_J$ results in Figure 5,

the growth rate is higher because w is smaller. We conclude that the disk eccentricity growth is possible over $\sim 10^3$ orbits in the case of planets because of contributions from several resonances that lie in the disk edge/gap region. This situation differs from the superhump binary case where only a single resonance is involved, since the disk extends relatively closer to the perturber in the planet case, due to its weaker tidal barrier.

Increased viscosity affects the disk eccentricity in multiple ways. It leads to further disk penetration of the planet's tidal barrier, which could lead to stronger eccentricity growth. On the other hand, viscosity also acts to unsaturate (or strengthen) the corotation resonances which act to damp eccentricity. Furthermore, the viscosity acts to damp the non-circular motions associated with the eccentricity.

5. Planet Orbital Evolution

At time $t = t_{\text{rls}}$ (between 1000–1200 orbits) the planet was allowed to adjust its orbit in response to the gravitational forces exerted by the surrounding disk material. We generally neglected torques on the planet due to gas within a distance of $0.5 R_H$ from the planet. However, analyses of the torque distribution at the release time indicate that torques within the Roche lobe do not dominate the orbital evolution of the planet. So we believe this procedure does not likely lead to major errors in the planet's orbital evolution. All calculations presented in this section employed grid GS2, except for the $3 M_J$ cases on initially circular orbits ($e_0 = 0$), which employed grid GS1. In order to analyze the orbital evolution of the planet after release, we calculated the osculating elements of the orbit each few hydrodynamics time-steps (approximately every 0.01 orbits). To remove short-period oscillations, we computed the mean orbital elements (Beutler 2005) by using an averaging period of one orbit. Throughout the paper, the planetary orbital eccentricities and semi-major axes in the simulations refer to the mean orbital elements.

5.1. Orbital Eccentricity

Simulations by Papaloizou et al. (2001) showed that the interaction between an initially circular disk and a circular orbit planet with mass $\gtrsim 20 M_J$ can lead to the growth of disk eccentricity and planetary orbital eccentricity. They also found that this interaction can be more efficient at augmenting orbital eccentricity than direct wave excitation at the outer 1:3 Lindblad resonance in a non-eccentric disk (e.g., Artymowicz 1992). We aim at determining whether a similar phenomenon can occur also in the Jupiter-mass range.

Figure 8 shows that the interaction between a planet and a disk leads to orbital eccentricity growth for the $2 M_J$ (dashed line) and $3 M_J$ (solid line) cases. During the initial growth of e for the $3 M_J$ planet, the rate is $\dot{e} \approx 1.3 \times 10^{-4} \text{ orbit}^{-1}$. This value is ~ 1.6 times that exhibited by the $2 M_J$ planet. The eccentricity growth stalls when $e \simeq 0.08$ for both planet

except that the magnitude of $S_{(1,0)}$ in the innermost region is about a factor of 8 smaller. The average growth rate of $S_{(1,0)}$ in the innermost region is about the same over 1000 orbits.

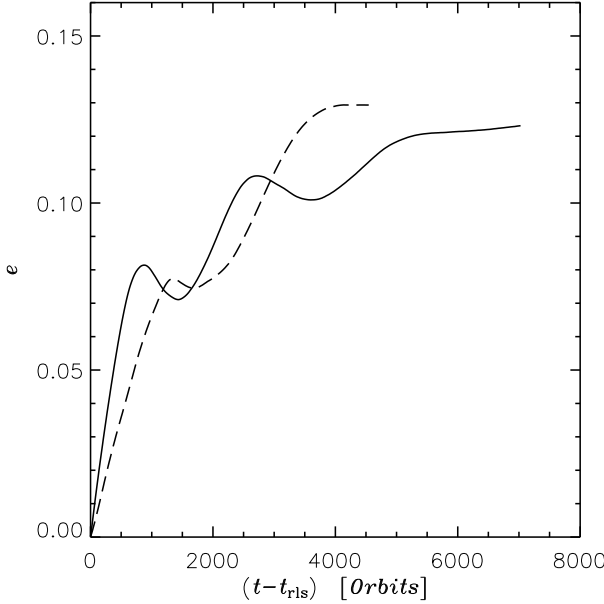


Fig. 8.— Evolution of the (mean) orbital eccentricity of $2 M_J$ (dashed line) and $3 M_J$ (solid line) planets after the release time, $t_{\text{rls}} = 1000$ orbits.

masses. The planets may be experiencing some variation in their eccentricity forcing due to the phasing of their eccentricities relative to the disks'. After 1500–1600 orbits from the release time, the orbital eccentricity starts to increase again with a growth timescale that is comparable to the initial growth timescale, $\tau_E \equiv e/|\dot{e}| \approx 2.3 \times 10^3$ orbits, for both planetary masses. The average growth timescale is shorter than the standard Type II migration (or viscous diffusion) timescale (see § 5.2). Over the last 1000 orbits of the simulation, the eccentricity of the $3 M_J$ planet increases very slowly, at a rate $\dot{e} \approx 2 \times 10^{-6}$ orbit $^{-1}$.

The model with $M_p = 1 M_J$ and initial zero-eccentricity (Fig. 9, dashed line) shows a much slower orbital eccentricity growth, reaching $e = 0.02$ after 3000 orbits from the release time. As described in Section 4.3, the eccentric perturbation induced by the planet on the disk is also rather weak compared to that excited by the $2 M_J$ planet. At the average growth rate $\dot{e} \approx 7 \times 10^{-6}$ orbit $^{-1}$, it would take on the order of the viscous diffusion timescale to reach $e \approx 0.1$.

In order to evaluate to the extent of orbital eccentricity growth, we used configurations with fixed non-zero planet eccentricities prior to release, e_0 . Figure 9 also shows the orbital eccentricity evolution of a $M_p = 1 M_J$ planet with $e_0 = 0.01$. After release, e oscillates about the initial value. The oscillation grows in amplitude and, during one of these cycles, e increases from 0 to 0.09 within about 1300 orbits. In this case, τ_E is of order the viscous diffusion timescale. We simulated several models with $e_0 \geq 0.1$ (not plotted) and found that there was generally a reduction of the orbital eccentricity, with some exceptions though. For example, in a model

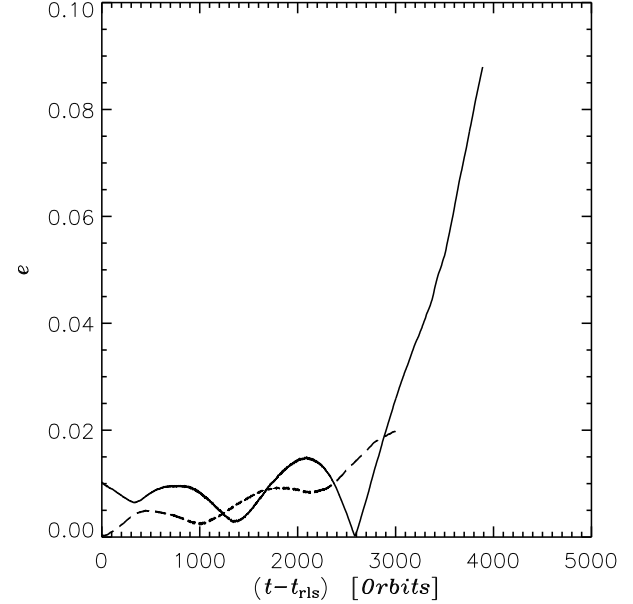


Fig. 9.— Orbital eccentricity versus time of Jupiter-mass models with different initial orbital eccentricities: $e_0 = 0$ (dashed line) and $e_0 = 0.01$ (solid line). The release time is 1100 orbits.

with a $1 M_J$ planet and $e_0 = 0.1$, e underwent small amplitude oscillations about the initial value, with periods of a few hundred orbits. This occurrence may be related to the relatively large eccentricity driven in the outer disk. Some models with $e_0 \geq 0.2$ showed a rate of change of e that diminishes in time. In these cases the evolution was generally monitored for less than 1000 orbits. Longer time coverage simulations are required to assess the long-term behavior of these configurations.

5.2. Radial Migration

We describe here some results on the migration of eccentric orbit planets. We plan to explore this issue further in a future paper. Radial migration of planets in the mass range considered in this study is expected to be in the standard Type II regime, which is characterized by an orbital decay timescale $\tau_M \equiv a_0/|\dot{a}| = 2a_0^2/(3\nu) = \tau_M^{\text{II}}$ (Ward 1997). The Type II migration rate depends only on the viscous timescale of the disk near the location of the planet and is independent of the disk density, provided the disk is locally more massive than the planet. Type II migration is based on the assumption that the gap, which separates the inner and outer disks, is devoid of material. In this case, the planet torques approximately balance the viscous torques at the gap edges.

Figure 10 plots the evolution of the semi-major axes, after the release time, of models with three planetary masses: $M_p = 1 M_J$ (short-dashed line), $M_p = 2 M_J$ (long-dashed line), and $M_p = 3 M_J$ (solid line). The Figure shows that the initial migration rate depends on the planet's mass, which is

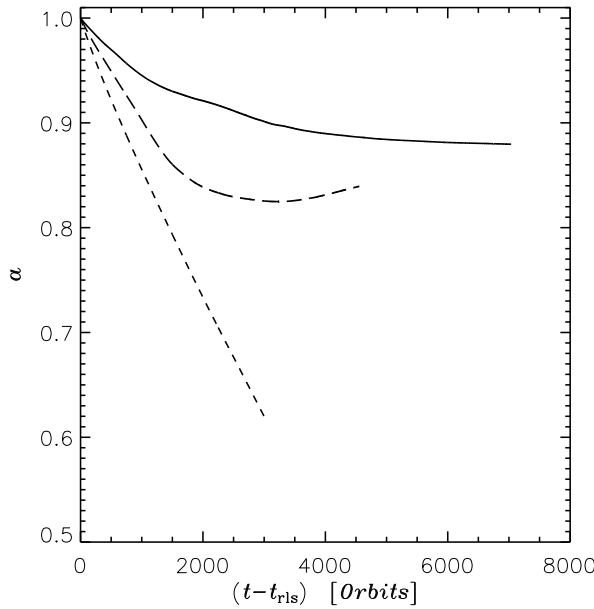


Fig. 10.— Evolution of the semi-major axis of planets: $M_p = 1 M_J$ (short-dashed line), $M_p = 2 M_J$ (long-dashed line), and $M_p = 3 M_J$ (solid line). The release time is about 1000 orbits. The initial eccentricity $e_0 = 0$ in the 3 cases. The change in migration rates for the $2 M_J$ and $3 M_J$ cases at later times is related to their increased orbital eccentricity (see Figure 8).

inconsistent with the Type II prediction. We may expect some dependence of the migration rate on planet mass, because ratio of planet to disk mass is non-zero (Syer & Clarke 1995; Ivanov et al. 1999). In order to explore this result further, we have used a one-dimensional disk evolution code, along the lines of Lin & Papaloizou (1986). We used the torque density per unit mass given in equation (4) of Lubow & D'Angelo (2006). We checked that the results are insensitive to the details of the torque density, provided that it is large enough to produce a gap. Increasing the torque density everywhere by a factor of 2 produced a small change in the migration rate (less than 1%). We adopted the same disk and planet parameters as in the two-dimensional simulations with zero planet eccentricity. In short, we find that the largest contributing factor to this non-Type II behavior is the lack of a substantial inner disk in the two-dimensional calculations. There is also some effect due to the non-zero planet-to-disk mass ratio.

A comparison of orbital migration between one-dimensional and two-dimensional models is shown in Figure 11. In this comparison we used the azimuthal averaged surface density distributions in Figure 2 as initial conditions for the one-dimensional models. As seen in Figure 11, the one-dimensional (zero eccentricity) migration rates, for a very low density inner disk, agree well with the two-dimensional rates at early times after release, while the planet eccentricity is small. For undepleted initial inner disks, we find that one-dimensional models have about the same migration rates

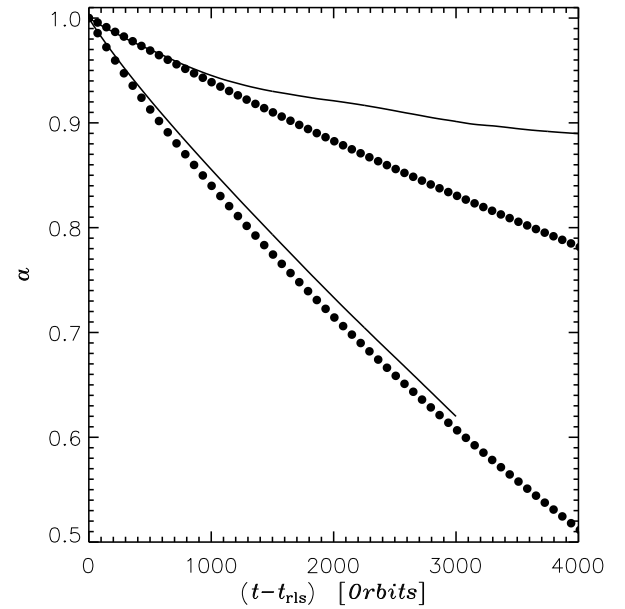


Fig. 11.— Orbital migration of a $1 M_J$ and a $3 M_J$ planet according to one-dimensional simulations (dots) and two-dimensional simulations (lines) that use the same disk and planet parameters. The two upper curves are for the $3 M_J$ planet. The one-dimensional simulations have an initially depleted inner disk, whose density distribution matches that of the two-dimensional simulations at planet release. Note the good agreement between one-dimensional and two-dimensional simulations for the $1 M_J$ planet. The agreement is also very good for the $3 M_J$ planet, as long as its eccentricity is smaller than about 0.1 (see Fig. 8). Planet orbits are assumed to always be circular in the one-dimensional models.

for these two planet masses. It is possible that the two-dimensional simulations have an inner boundary r_{\min} that is too large to resolve the inner disk. More complete zone coverage of the inner region in the two-dimensional calculations might reveal an inner disk that acts to make the migration rate less dependent on mass, as indicated by the one-dimensional simulations. In spite of these possible limitations of our two-dimensional simulations, we describe below some interesting aspects of the migration of eccentric orbit planets in two-dimensional disks.

As a planet's orbital eccentricity grows toward values of about 0.08, the rate of migration slows significantly (see Fig. 10). Over the last 1000 orbital periods of the calculated evolution, the $3 M_J$ planet exhibits a migration speed $\dot{a} \approx -2 \times 10^{-6} a_0$ per orbit, with a tendency towards further reduction. This migration rate is about a factor of 30 smaller than the rate at release time. The $2 M_J$ shows an even more drastic reduction of the migration rate that actually reverses and becomes positive around $t - t_{rls} \approx 4200$ orbits. The outward migration speed is $\dot{a} \approx 1 \times 10^{-5} a_0$ per orbit at the end of the simulation. The migration speed of the $1 M_J$ planet

($e_0 = 0$) is much more constant over the course of the simulation as its orbital eccentricity remains small ($e \lesssim 0.02$). The migration of a $1 M_J$ with $e_0 = 0.01$ proceeds as indicated by the short-dashed line in Figure 10. Over the last ≈ 1000 orbits of evolution, however, the migration rate undergoes a decrease by a factor ≈ 2 . During that time, the eccentricity grows to 0.09 (see solid line in Fig. 9).

The effect of non-zero orbital eccentricity on planet migration can also be seen in Figure 12, where the evolution of the semi-major axis is plotted for simulations with $M_p = 1 M_J$ and $M_p = 3 M_J$ and different initial orbital eccentricities. There is a clear trend towards slower migration rates for larger orbital eccentricities. In particular, when $e_0 \gtrsim 0.2$, the direction of migration is reversed. In all the calculations that show outward migration, the angular momentum of the eccentric orbit planet increases in time.

We have conducted some preliminary investigations on the cause of this outward torque. One possibility is that it is due to the outer disk, as suggested in Papaloizou (2002). When the planet eccentricity is large enough, the angular motion of the planet at apocenter can be slower than that of the inner parts of the outer disk, resulting in form of dynamical friction that increases the angular momentum of the planet. For the situation we wish to consider, it is not clear how the outer disk inner edge is maintained, when this model is applied. This disk material loses angular momentum from viscous torques and gains angular momentum from the planet, in the usual torque balance for a gap. The latter implies that the planet should lose, rather than gain, angular momentum.

A preliminary analysis suggests that the outward torque may arise in the coorbital region. This region is supplied by material that flows from the outer disk across the gap, as discussed in Section 6. In any case, further analysis is required to understand this situation.

We conducted a convergence test on the model with a $1 M_J$ planet and $e_0 = 0.2$, which exhibits outward migration. The test involved a comparison of the migration rates obtained from the grid system GS2 (see Table 2) to those obtained from a grid system whose linear resolution was a factor 1.3 larger everywhere (in both directions on each grid level). However, since computing resources were only available to run the higher resolution simulation for about 700 orbits, we used the Gauss perturbation equations (e.g., Beutler 2005) to compute \dot{a} resulting from the disk's gravitational forces, while keeping the planet's orbit fixed. The result of the test is that the migration rates, averaged from 200 to 700 orbits, differed by only 7% at the two resolution levels. As a check on our use of the Gauss equation, we also compared the migration rate determined from the Gauss equation, averaged over the last 100 orbits before release, to the initial \dot{a} after release, evaluated by integrating the equations of motion of the planet (see the left panel of Figure 12). The two rates, both determined on grid system GS2, differed by less than 3%.

5.3. Effects of Viscosity

As we discussed in Section 4.3.1, the disk eccentricity decreases with viscosity. For a coupled disk-planet system, we

similarly expect that the planet eccentricity would decrease with α , since the eccentric corotation resonances become stronger. The orbital eccentricity evolution of $3 M_J$ planets in disks with different α values is shown in the top-left panel of Figure 13. The model with standard viscosity (solid line) is the same as that in Figure 8. Over a period of 2200 orbits, the orbital eccentricity of the model with $\alpha_0 = 1.2 \times 10^{-2}$ (short-dashed line) remains small and never exceeds $e \approx 0.01$. On the other hand, the models with lowest viscosities, $\alpha_0 = 1.2 \times 10^{-3}$ (long-dashed line) and 4×10^{-3} exhibit a generally growing eccentricity. The trend towards faster growth for smaller viscosities is confirmed by the model with $1 M_J$ and $\alpha_0 = 1.2 \times 10^{-3}$, as indicated by the long-dashed line in the bottom-left panel of Figure 13.

The orbital evolution of the semi-major axis of $3 M_J$ planets for the three disk viscosities is displayed in the top-right panel of Figure 13. The radial inward migration is faster for larger α , as expected in a Type II-like regime. The plot supports the contention that planet eccentricity slows migration. Around 4000 orbits after the release time, the two calculations with smallest viscosities ($\alpha_0 = 4 \times 10^{-3}$ and 1.2×10^{-3}) produce migration rates respectively equal to $\dot{a} \approx -8 \times 10^{-6} a_0$ ($e \approx 0.11$) and $\dot{a} \approx -3 \times 10^{-6} a_0$ ($e \approx 0.14$) per orbit. The first rate is a factor 8 smaller, while the second a factor 13 smaller, than the initial migration speed (i.e., when $e \approx 0$). For these cases, the average eccentricity growth rate at a time of about 2500 orbits is $\dot{e} \approx 2 \times 10^{-5} \text{ orbit}^{-1}$. The migration of a $1 M_J$ planet (Fig. 13, bottom-right panel) also shows that, as the orbital eccentricity approaches ~ 0.08 , $|\dot{a}|$ starts to reduce. When $\alpha_0 = 1.2 \times 10^{-3}$, the average migration rate, over the last 1000 orbits, is about a factor 5 smaller than it is during the first 1000 orbits of evolution after release.

6. Pulsed Accretion

For eccentric orbit binary star systems, the accretion from a circumbinary disk onto the stars pulsates over the orbital period of the binary (Artynowicz & Lubow 1996; Günther & Kley 2002). This effect is related to the pulsating character of the equipotential surfaces of the elliptical restricted three-body problem (Todoran 1993).

We measured the mass accretion rate (which we denote as \dot{M}_p) into the inner portion of the planet's Roche lobe (within $r_{\text{acc}} = 0.3 R_H$), following the prescription described in Section 3.2, as a function of the planet's orbit phase. We refer to this rate as the planet accretion rate although the flow is not resolved on the scale of the planet's radius and thus the rate at which the planet would accrete mass may be modulated somewhat differently from \dot{M}_p . Quantity \dot{M}_p was determined by folding the mass accretion rate over planet orbital phase and averaging over 500 orbital periods (from 500 to 1000). Figure 14 shows the resulting averaged accretion rate, $\langle \dot{M}_p \rangle$, for $1 M_J$ and $3 M_J$ planets, versus the true anomaly (i.e., the azimuthal position relative to pericenter) of the planet and as a function of the orbital eccentricity. The simulations show pulsed accretion in cases of eccentric orbit planets. The amplitude of the variability, and to a lesser extent the phase, of \dot{M}_p depends on the orbital eccentricity.

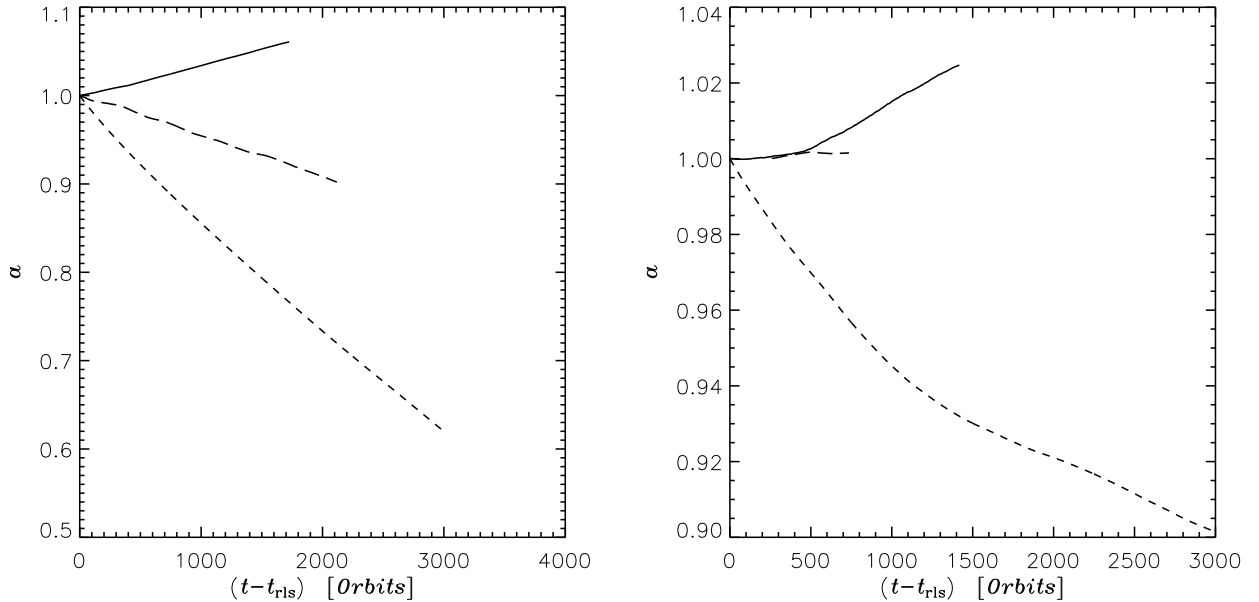


Fig. 12.— Left. Semi-major axis evolution of $1 M_J$ planets for three values of the orbital eccentricity at release: $e_0 = 0$ (short-dashed line), $e_0 = 0.1$ (long-dashed line), and $e_0 = 0.2$ (solid line). Right. Same as the left panel but for $3 M_J$ planets with orbital eccentricities at release: $e_0 = 0$ (short-dashed line), $e_0 = 0.2$ (long-dashed line), and $e_0 = 0.3$ (solid line). The release time is between 1000 and 1200 orbits. Our standard disk parameters were used, including $\alpha = 4 \times 10^{-3}$.

6.1. Modulation

The accretion onto a $1 M_J$ planet with $e = 0.1$ has two asymmetric peaks, the taller of which is around the apocenter position (true anomaly equal to π). The secondary peak is about 70% of the primary peak and is located close to the pericenter position. For $e \leq 0.2$, the modulation of \dot{M}_p increases with e . For larger orbital eccentricities, modulation decreases. This effect may be a consequence of the gap becoming broader and shallower with increasing e (see Fig. 2).

A similar phase variability is found for the mass accretion onto a $3 M_J$ planet (Figure 14, right panel). Even when the planet's orbit is circular, $\langle \dot{M}_p \rangle$ smoothly varies between $1.5 \times 10^{-4} M_J$ and $4.5 \times 10^{-4} M_J$ per orbit. The phasing in this case is arbitrary, since the planet's orbit is circular. This behavior is related to the eccentricity of the disk. The mass accretion is markedly peaked around the apocenter position when $e > 0.1$. The mass accretion modulation is again greatest for $e = 0.2$. When the planet eccentricity is between $e = 0.3$ and 0.4 , the highest accretion rate occurs roughly 0.1 orbits after apocenter. This delay may be related to the time required by material to be captured once it has been perturbed near the apocenter. Due to such a delay, accretion on binaries occurs near pericenter (Artymowicz & Lubow 1996).

The density distribution in the vicinity of an eccentric orbit planet varies strongly with its orbital phase. This variation is illustrated in the panels of Figure 15, which depict the situation at the pericenter (left) and apocenter (right), for a $1 M_J$ (top) and a $3 M_J$ planet (bottom) on an eccentric orbit with $e = 0.2$. The spiral waves have a regular pattern at pericenter,

when the planet is orbiting in the low-density gap (or cavity). As the planet approaches the apocenter, the outer spiral wake penetrates higher density regions, which causes fluid elements along the wake to lose angular momentum and flow through the gap. There are streams of material that extend inwards (at $r < a$ and $\phi > \phi_p$) which appear in the right panels of Figure 15.

6.2. Mass Growth Timescale

The mass accretion rate onto a planet with a fixed circular orbit decreases with increasing planet mass when $M_p \gtrsim 1 M_J$ (Lubow et al. 1999). The average accretion rate in the simulations, at $t \simeq 150$ orbits, of a $2 M_J$ planet is 0.63 times that of a $1 M_J$ planet. The ratio decreases to 0.44 for a $3 M_J$ planet on a circular orbit and at $t = 150$ orbits. These ratios agree within 10% with the values given by Lubow et al. (1999), who used an independent code.

As the disk eccentricity grows, the mass accreted during an orbit increases. At later times $t \gtrsim 500$ orbits, when $S_{(1,0)} \gtrsim 0.2$, the accretion rate onto a $2 M_J$ planet is 0.71 times the rate onto a $1 M_J$ planet and for a $3 M_J$ planet is 0.65 times the rate onto a $1 M_J$ planet. Notice that, for a $3 M_J$ planet, this implies a 48% increase over the accretion rate at early stages, when the disk is circular. These results suggest that the eccentricity driven in the disk by a massive planet can augment the mass accretion rate onto the planet and hence shorten its growth timescale.

Mass accretion over an orbit period can also be enhanced by the planet's orbital eccentricity. For a $1 M_J$ planet on a

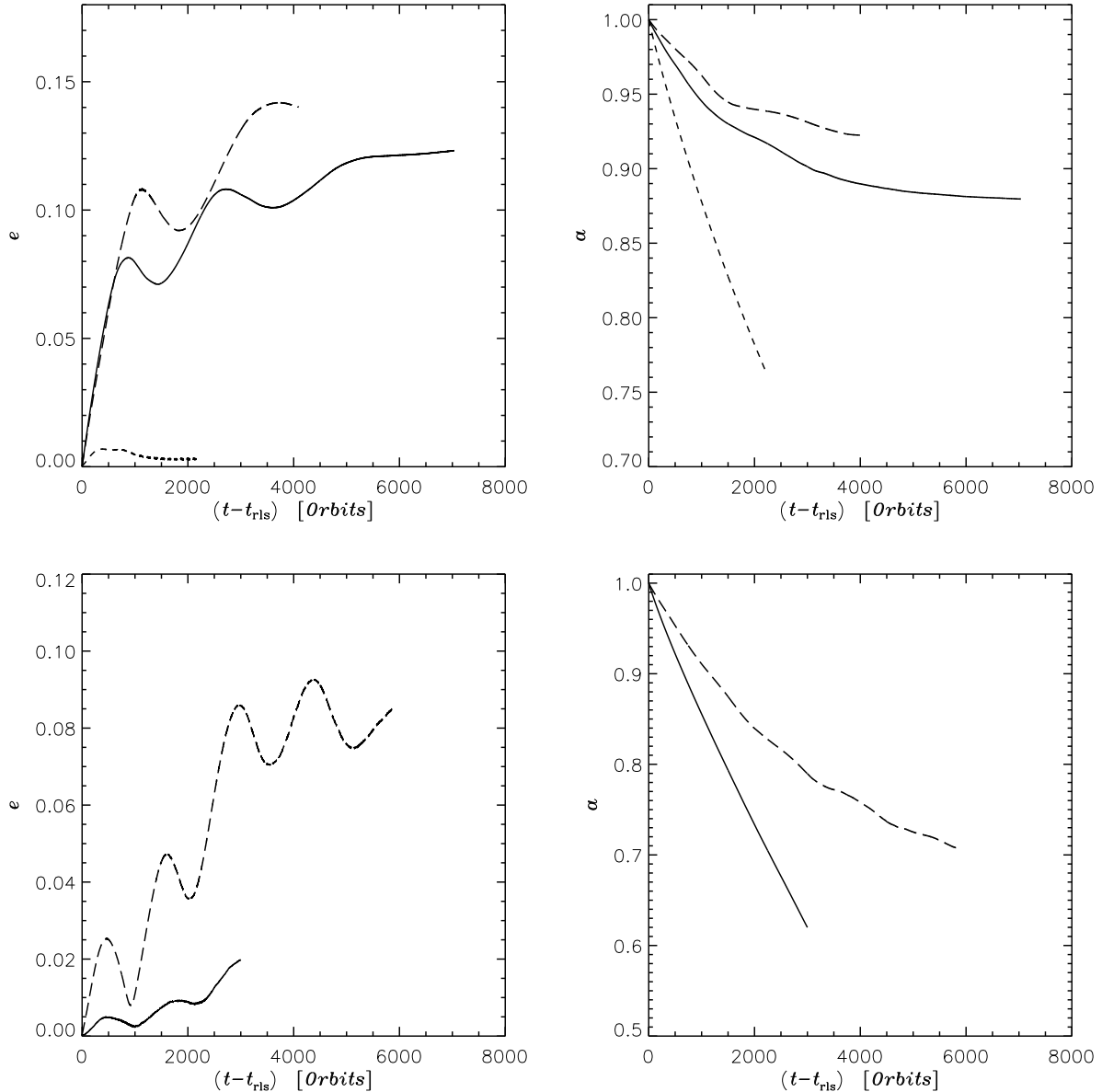


Fig. 13.— Evolution of planet eccentricity (left) and semi-major axis (right) for $3 M_J$ (top) and $1 M_J$ (bottom) planets in disks with different values of viscosity parameter α_0 (α at $r = a_0$), $\alpha_0 = 1.2 \times 10^{-3}$ (long-dashed line), $\alpha_0 = 4 \times 10^{-3}$ (solid line), and $\alpha_0 = 1.2 \times 10^{-2}$ (short-dashed line). The release time is $t_{rls} = 1000$ orbits in the top panels and 1100 orbits bottom panels.

fixed orbit, the mass growth timescale (defined here as the ratio of M_p to the average accretion rate between 500 and 1000 orbits) decreased by about 35% when e is increased from 0 to 0.2. The reduction of mass growth timescale from $e = 0$ to $e = 0.4$ is only 17%, perhaps as a result of the wider gap and its smoother outer edge at larger orbital eccentricities (see Fig. 2). For a $3 M_J$ planet on a fixed orbit with $e = 0.3$, the mass growth timescale is reduced relative to the $e = 0$ case by 27%. While for $e = 0.4$ there was a 13% reduction. For cases with $e < 0.3$, the growth rate was not substantially different than the $e = 0$ case.

The mass growth timescale of a $1 M_J$ and a $3 M_J$ planet on circular orbit was also estimated for different values of the disk viscosity. For a $3 M_J$ planet an increase in α by a factor of 3 over the standard value (see § 2.2) reduced the growth timescale by about 60%. For both planetary masses, a decrease in α by a factor of 3.3 below the standard value, lengthened the growth timescale by a factor 2.

Planetary accretion rates were determined by means of the grid system GS2. Simulations executed with grid systems GS1 and GS3 resulted in very similar outcomes (within 6%)

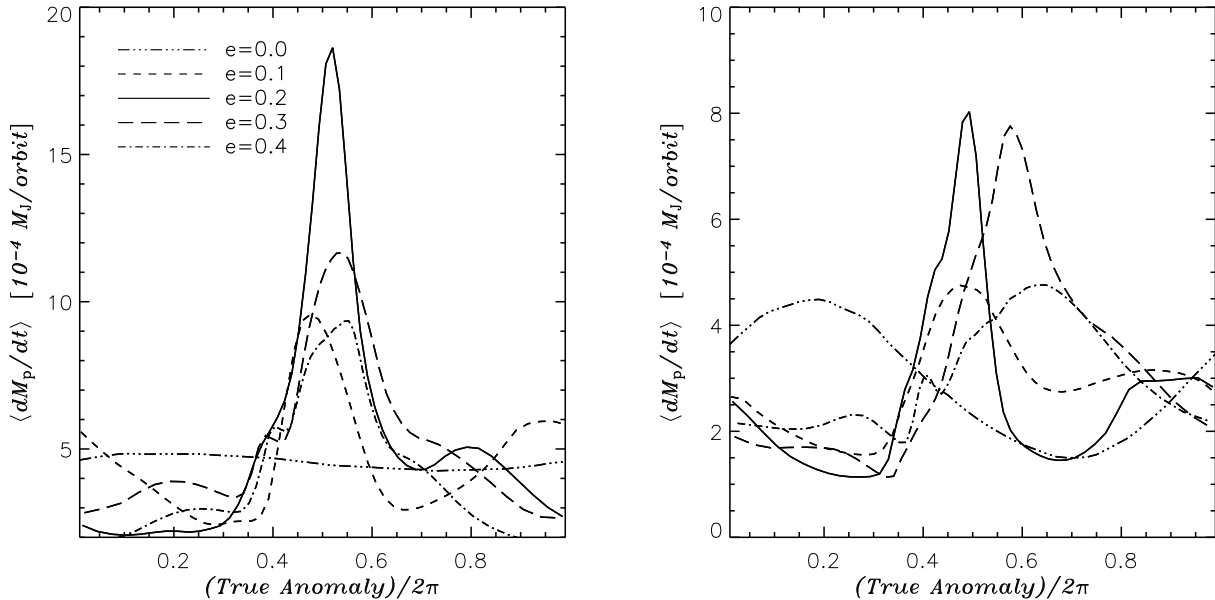


Fig. 14.— Mass accretion rate in inner parts of the Roche lobe of a $1 M_J$ (left) and a $3 M_J$ (right) planet as a function of its true anomaly and orbital eccentricity. When the true anomaly equals π , the planet is located at the apocenter of the orbit. Orbital eccentricities are listed in the legend of the left panel. The quantity $\langle \dot{M}_p \rangle$ is obtained by sampling \dot{M}_p every 0.02 orbits and averaging the outcome from 500 to 1000 orbits.

for both the modulation of \dot{M}_p and its average value. The results are not sensitive to the smoothing length, ε , although this parameter can affect the small-scale structure of the flow around the planet. We performed a calculation for an ε value that was reduced by a 25%, with $M_p = 3 M_J$ and $e = 0.3$, and obtained essentially the same accretion rates (within 1%).

6.3. Accretion towards the Star

The region interior to a planet's orbit likely contains an inner disk which cannot be resolved in the current two-dimensional simulations (see discussion in § 5.2). We estimate the modulation of mass onto this disk as a function of orbital phase by considering the mass flow rate across the inner boundary. As material accretes through the inner disk, the modulation would be expected to weaken. It is unclear whether the modulation would be reflected as a variable accretion at the surface of the star. Perhaps it could be manifested as variability in emission from the region where the inflow meets the outer edge of the inner disk.

Figure 16 plots the accretion rate at the inner boundary $\langle \dot{M}_* \rangle$ versus the true anomaly of the planet for cases with $M_p = 1 M_J$ and $3 M_J$. The case involving the more massive planet produces an accretion rate through the inner boundary that is largest when the planet is close to the apocenter. The maximum of $\langle \dot{M}_* \rangle$ occurs before the apocenter passage for the case involving the $1 M_J$ planet. The average mass accreted by the star during one orbital period of the planet is $5.8 \times 10^{-8} M_*$ and $9.9 \times 10^{-8} M_*$ for the $1 M_J$ and the $3 M_J$ cases, respectively. The same models with no orbital eccen-

tricity show relatively constant $\langle \dot{M}_* \rangle$ values of $1 \times 10^{-7} M_*$ ($M_p = 1 M_J$) and $6.3 \times 10^{-8} M_*$ ($M_p = 3 M_J$) per orbit. As a comparison, the mass accretion through a steady-state α -disk is $3\pi\Sigma\nu$ (Lynden-Bell & Pringle 1974; Pringle 1981) which, using the initial unperturbed surface density and standard viscosity ($\alpha_0 = 4 \times 10^{-3}$), yields $2.5 \times 10^{-7} M_*$ per orbit or $2 \times 10^{-8} M_\odot \text{ yr}^{-1}$.

The ratio of the accretion on the star to the accretion in the disk, outside the gap, can be expressed as $\langle \dot{M}_* \rangle_o / (\langle \dot{M}_* \rangle_o + \langle \dot{M}_p \rangle_o)$, where the subscript “o” denotes the integral of the respective accretion rate over a planetary orbit. For both the $1 M_J$ and the $3 M_J$ planets on circular orbit, this ratio is 0.19. When $e = 0.2$, the ratio is 0.09 and 0.26 for the $1 M_J$ and the $3 M_J$ planet, respectively. The reduced mass transfer across the planet's orbit, when $M_p = 1 M_J$ and $e = 0.2$, can be attributed to the increased accretion rate onto the planet, as reported above. In the $3 M_J$ case, $\langle \dot{M}_p \rangle_o$ does not vary significantly as e varies from 0 to 0.2. Instead, the mass flux across the gap is likely enhanced by the radial excursion of the planet (see § 6).

7. Summary and Discussion

We simulated the orbital evolution of circular and eccentric orbit giant planets embedded in circumstellar disks. The disks were analyzed using a two-dimensional hydrodynamics code that utilizes nested grids to achieve high resolution in a large region ($2a \times 2\pi/3$) around the planet. The disks were modeled as an α -disk and a few values of α were considered. We investigated planet masses of $1 M_J$, $2 M_J$, and $3 M_J$ and

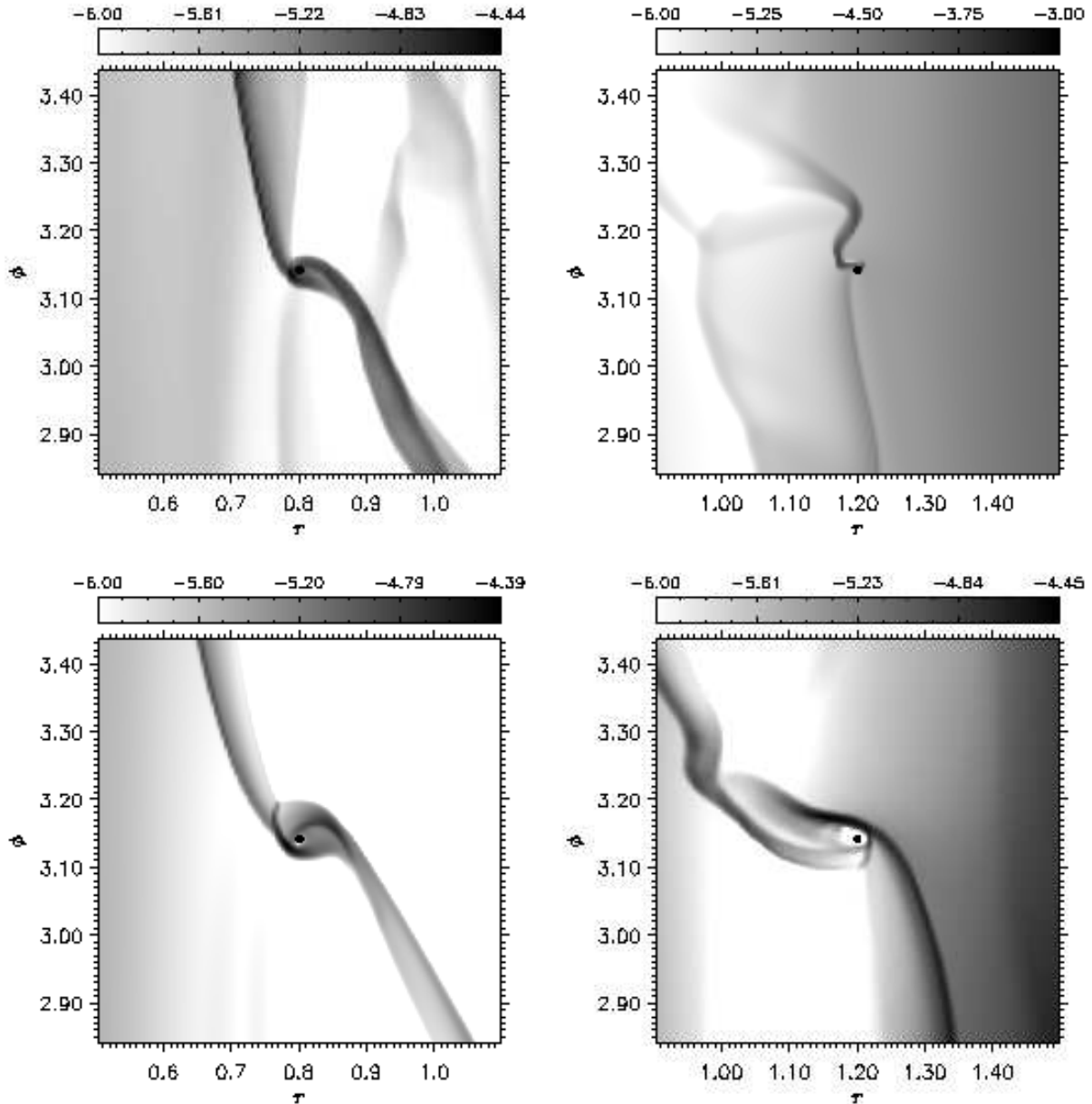


Fig. 15.— Density structure around a $1 M_J$ (top) and a $3 M_J$ (bottom) planet at pericenter (left) and apocenter (right). The vertical axis is the azimuth about the star and the horizontal axis is the distance from the star in units of a_0 . The orbital eccentricity is $e = 0.2$ and $t \simeq 1000$ orbits. The solid circle indicates the instantaneous location of the planet. A surface density of 10^{-5} corresponds to 3.29 g cm^{-2} .

initial orbital eccentricities that ranged from 0 to 0.4.

Disk gaps become broader and shallower as the planet eccentricity increases (see Fig. 1 and 2). The density near the orbit of the planet is very small compared with the density in the disk for all eccentricities considered. A planet on a fixed circular orbit can cause an initially circular disk to become eccentric (see Fig. 4). The disk eccentricity is suppressed at lower planet masses ($M_p \lesssim 1 M_J$) and higher disk viscosities ($\alpha \gtrsim 0.01$), as also found by Kley & Dirksen (2006) and by

Papaloizou et al. (2001) at higher planet masses. We attribute the eccentricity growth to a tidal instability associated with a series of eccentric outer Lindblad resonances in the inner parts of the outer disk (Fig. 7). The same type of instability, involving an inner disk, is thought to be responsible for the superhump phenomena in binary star systems (Lubow 1991a; Osaki 2003).

The simulations indicate that planet eccentricity can grow, as a consequence of disk-planet interactions (Fig. 8 and 9).

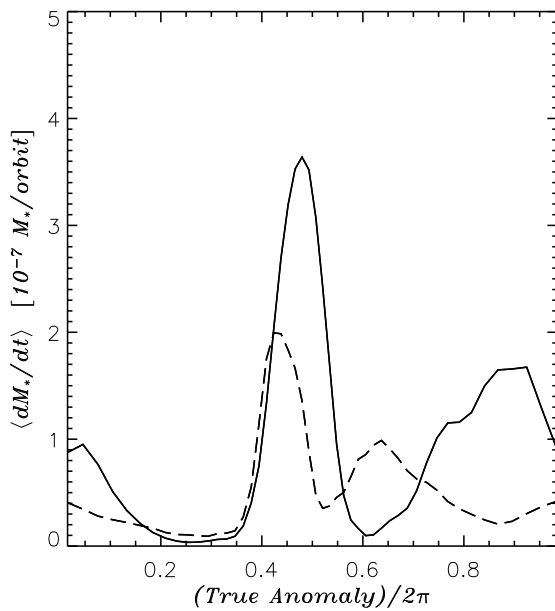


Fig. 16.— Mass accretion rate towards the star at the inner boundary $r = 0.3 a_0$ as function the true anomaly of the planet. The mass accretion rate is averaged over several planet orbital periods at $t \approx 1000$ orbits. The dashed and solid lines refer to models with $M_p = 1 M_J$ and $3 M_J$, respectively. The planet's orbital eccentricity is $e = 0.2$. When the true anomaly is π , the planet is located at the apocenter.

The growth is stronger in the $2 M_J$ and $3 M_J$ cases than for $1 M_J$, and for lower disk viscosity ($\alpha \lesssim 4 \times 10^{-3}$). Planet eccentricities of ~ 0.1 were found in the simulations over the course of a few thousand orbits for $2 M_J$ and $3 M_J$ planets. A similar eccentricity growth is obtained for a $1 M_J$ planet in a disk with viscosity $\alpha \approx 10^{-3}$. The planet and disk both acquire eccentricity as they interact, which may lead to complicated time-dependent behavior of their eccentricities. The planet eccentricity growth is likely aided by the disk eccentricity growth. The results suggest that the eccentric growth found for $\sim 10 M_J$ planets by Papaloizou et al. (2001) also occurs for lower planet masses. The higher resolution achieved by our calculations may be playing a role in obtaining this growth.

For circular orbit planets, migration occurs on roughly the local viscous timescale, as expected for Type II migration. However, it is slowed for eccentric orbit planets. This result appears for several configurations with either dynamically determined (Fig. 10 and 13) or imposed planet eccentricities (Fig. 12). For a $2 M_J$ case, even migration reversal (outward migration) is found for a dynamically determined eccentricity (Fig. 10). Migration slowing or reversal would have important consequences for the planet formation process. The cause is not yet clear. It may involve torques from outer disk (Papaloizou 2002) or instead from the coorbital region. Some preliminary evidence suggests the latter.

Mass accretion both within a planet's Roche lobe and through a gap can be strongly modulated with orbital phase for eccentric orbit planets or eccentric disks (Fig. 14, 15, and 16). The modulation was largest for planet eccentricity $e \simeq 0.2$. This pulsating accretion is similar to what is found for eccentric orbit binary stars embedded in a circumbinary disk (Artymowicz & Lubow 1996), although the phasing is different. Both disk and planet eccentricity also lead to enhanced accretion onto the planet. This enhancement likely helps planets achieve higher masses.

The simulations lend support to the idea that disk-planet interactions cause planet eccentricity growth, along the lines of Goldreich & Sari (2003). The simulations suggest that planet eccentricities are easier to achieve for higher mass planets ($M_p \gtrsim 2 M_J$). Our results are subject to the usual limitations in approximate initial conditions, simulation time, radial range for coverage of the disk (likely resulting in the lack of an inner disk), the α -disk model, and the use of various numerical devices. We also neglected disk self-gravity, which may affect migration especially for higher mass disks (Nelson & Benz 2003a).

However, it is not clear that typical extra-solar planet eccentricities of 0.2–0.3 can be achieved through disk-planet interactions. The eccentricity growth at later times shows indications of slowing and possibly stalling for $e \lesssim 0.15$ (see Fig 13.) Perhaps higher eccentricities can be achieved for disks with different properties (e.g., lower viscosity and smaller disk's aspect ratio). Eccentricity may be limited by damping due to high order eccentric inner Lindblad resonances that lie outside a planet's orbit. Simulations of eccentric orbit binary star systems suggest that little eccentricity growth occurs for $e \gtrsim 0.5$ (Lubow & Artymowicz 1992). Although the simulated planets do not achieve orbital eccentricities in excess of 0.15 over the duration of the simulated evolution (for configurations that start from circular orbits), the simulation times correspond to less than 10^5 years. Migration slowing and reversal may permit the planets to achieve higher eccentricities on longer timescales while avoiding orbit decay into the disk center/host star.

We have not yet investigated eccentricity evolution of sub-Jupiter mass planets. They may also provide important constraints. Other simulations suggest that disks with standard viscosity have only mild gaps for smaller planet masses of $M_p \lesssim 0.1 M_J$ (e.g., D'Angelo et al. 2003; Bate et al. 2003). Under those conditions, disk-planet interactions likely lead to eccentricity damping, due to the dominance of the coorbital Lindblad resonance (Ward 1986; Artymowicz 1993). The observational determination of eccentricities for small mass planets would help constrain these models. The planet around HD 49674 is close to this regime. It has a minimum mass of $0.11 M_J$ and a best-fit eccentricity of 0.29 (P. Butler, private communication). Since it is close to the central star (the period is 4.9 days), it is possible that the eccentricity evolution could be more complicated, especially if it became trapped in a central disk hole. Examples of isolated planets like this, but at longer periods would provide useful constraints.

We thank Gordon Ogilvie and Jim Pringle for useful dis-

cussions. The computations reported in this paper were performed using the UK Astrophysical Fluids Facility (UKAFF). GD was supported by the Leverhulme Trust through a UKAFF Fellowship, by the NASA Postdoctoral Program, and in part by NASA's Outer Planets Research Program through grant 811073.02.01.01.20. SL acknowledges support from NASA Origins of Solar Systems grant NNG04GG50G. MRB is grateful for the support of a Philip Leverhulme Prize.

REFERENCES

Artymowicz, P. 1992, *PASP*, 104, 769

—. 1993, *ApJ*, 419, 166

Artymowicz, P., Clarke, C. J., Lubow, S. H., & Pringle, J. E. 1991, *ApJ*, 370, L35

Artymowicz, P., & Lubow, S. H. 1994, *ApJ*, 421, 651

—. 1996, *ApJ*, 467, L77

Bailey, J. M. 1972, *AJ*, 77, 177

Bate, M. R., Lubow, S. H., Ogilvie, G. I., & Miller, K. A. 2003, *MNRAS*, 341, 213

Beutler, G. 2005, Methods of celestial mechanics. Vol. I: Physical, mathematical, and numerical principles (Methods of celestial mechanics. Vol. I / Gerhard Beutler. In cooperation with Leos Mervart and Andreas Verdun. Astronomy and Astrophysics Library. Berlin: Springer, ISBN 3-540-40749-9, 2005, XVI, 464 pp. 99 figures, 11 in color, 32 tables and a CD-ROM.)

D'Angelo, G., Bate, M. R., & Lubow, S. H. 2005, *MNRAS*, 358, 316

D'Angelo, G., Henning, T., & Kley, W. 2002, *A&A*, 385, 647

D'Angelo, G., Kley, W., & Henning, T. 2003, *ApJ*, 586, 540

Ford, E. B., Havlickova, M., & Rasio, F. A. 2001, *Icarus*, 150, 303

Godon, P. 1996, *MNRAS*, 282, 1107

—. 1997, *ApJ*, 480, 329

Goldreich, P., & Tremaine, S. 1980, *ApJ*, 241, 425

Goldreich, P., & Sari, R. 2003, *ApJ*, 585, 1024

Goodchild, S., & Ogilvie, G. 2006, *mnras*, 368, 1123

Günther, R., & Kley, W. 2002, *A&A*, 387, 550

Ivanov, P. B., Papaloizou, J. C. B., & Polnarev, A. G. 1999, *MNRAS*, 307, 79

Juric, M., & Tremaine, S. 2005, American Astronomical Society Meeting Abstracts, 207,

Kley, W., D'Angelo, G., & Henning, T. 2001, *ApJ*, 547, 457

Kley, W., & Dirksen, G. 2006, *A&A*, 447, 369

Lin, D. N. C., & Papaloizou, J. 1986, *ApJ*, 309, 846

Lubow, S. H. 1991a, *ApJ*, 381, 259

—. 1991b, *ApJ*, 381, 268

—. 1992, *ApJ*, 401, 317

Lubow, S. H., & Artymowicz, P. 1992, in Binaries as Tracers of Stellar Formation. Proceedings of a Workshop held in Bettmeralp, Switzerland, Sept. 1991, in honor of Dr. Roger Griffin. Editors, Antoine Duquennoy, Michel Mayor; Publisher, Cambridge University Press, Cambridge, England, New York, NY, 1992. LC # QB821 .B55 1991. ISBN # 0521433584. P. 145, 1992, ed. A. Duquennoy & M. Mayor, 145

Lubow, S. H., & D'Angelo, G. 2006, *ApJ*, 641, 526

Lubow, S. H., Seibert, M., & Artymowicz, P. 1999, *ApJ*, 526, 1001

Lynden-Bell, D., & Pringle, J. E. 1974, *MNRAS*, 168, 603

Marcy, G., Butler, R. P., Fischer, D., Vogt, S., Wright, J. T., Tinney, C. G., & Jones, H. R. A. 2005, *Progress of Theoretical Physics Supplement*, 158, 24

Masset, F. S., & Ogilvie, G. I. 2004, *ApJ*, 615, 1000

Mihalas, D., & Weibel Mihalas, B. 1999, Foundations of radiation hydrodynamics (New York: Dover, 1999)

Nelson, A. F., & Benz, W. 2003a, *ApJ*, 589, 556

—. 2003b, *ApJ*, 589, 578

Nelson, R. P., & Papaloizou, J. C. B. 2004, *MNRAS*, 350, 849

Nelson, R. P., Papaloizou, J. C. B., Masset, F., & Kley, W. 2000, *MNRAS*, 318, 18

Ogilvie, G. I., & Lubow, S. H. 2003, *ApJ*, 587, 398

Osaki, Y. 1985, *A&A*, 144, 369

—. 2003, *PASJ*, 55, 841

Papaloizou, J. C. B. 2002, *A&A*, 388, 615

Papaloizou, J. C. B., & Nelson, R. P. 2003, *MNRAS*, 339, 983

Papaloizou, J. C. B., Nelson, R. P., & Masset, F. 2001, *A&A*, 366, 263

Pringle, J. E. 1981, *ARA&A*, 19, 137

Rasio, F. A., & Ford, E. B. 1996, *Science*, 274, 954

Shakura, N. I., & Sunyaev, R. A. 1973, *A&A*, 24, 337

Syer, D., & Clarke, C. J. 1995, *MNRAS*, 277, 758

Takeda, G., & Rasio, F. A. 2005, *ApJ*, 627, 1001

Tanigawa, T., & Watanabe, S. 2002, *ApJ*, 580, 506

Todoran, I. 1993, *Ap&SS*, 199, 257

van Leer, B. 1977, *JCP*, 23, 276

Ward, W. 1997, *Icarus*, 126, 261

Ward, W. R. 1986, *Icarus*, 67, 164

Winters, W. F., Balbus, S. A., & Hawley, J. F. 2003, *ApJ*, 589, 543

Wu, Y., & Murray, N. 2003, *ApJ*, 589, 605

Ziegler, U., & Yorke, H. W. 1997, *Computer Physics Communications*, 101, 54